J. Fluid Mech. (2013), *vol.* 714, *pp.* 361–392. © Cambridge University Press 2013
doi:10.1017/jfm.2012.481

'Effervescent' atomization in two dimensions

H. Lhuissier† and E. Villermaux‡

Aix-Marseille Université, IRPHE, 13384 Marseille CEDEX 13, France

(Received 5 February 2012; revised 27 September 2012; accepted 30 September 2012)

A planar Savart water sheet uniformly seeded with small air bubbles in a large surface concentration is studied as a model experiment of the so-called 'effervescent' atomization process. This two-dimensional setup allows for a quantitative observation of all the steps of the sheet's disintegration into a collection of disjointed droplets. The bubbles are heterogeneous nucleation sites which puncture the sheet with holes. The dynamics of the opening of holes competes with the simultaneous nucleation rate of new holes in a statistically stationary fashion. The liquid constituting the sheet is then transiently concentrated in a web of ligaments of various lengths and diameters, at the junction between adjacent holes. Their breakup produces the final spray. We provide a complete description of the ligament web statistics when nucleation is synchronous, and we show that the drop size dispersion from the breakup of a single ligament is responsible for the shape of the overall spray drop size distribution.

Key words: breakup/coalescence, drops and bubbles, interfacial flows (free surface)

1. Introduction

We explore the so-called 'effervescent' atomization process, in its two-dimensional version. The terminology 'effervescent' or 'aerated liquid' atomization, along with the corresponding technique, was introduced by Lefebvre in the late 1980s: see Sovani, Sojka & Lefebvre (2001) for a review. It consists in dispersing a minute fraction of a gas phase within the liquid to be atomized when the mixture is pressurized prior to its injection in a low-pressure chamber. As the pressure suddenly drops, the gas bubbles expand and fragment the liquid into small volumes, typically much smaller than those which would have been obtained if the same quantity of gas had been used to shear the liquid, as in common co-flow atomizers (Lefebvre 1989) such as coaxial jets (Marmottant & Villermaux 2004). This 'effervescent' process, though not yet routinely used (much less used than the 'aerators' of domestic taps injecting air into the jet by the Venturi effect to limit water consumption: see figure 2*a*), is thus a smart alternative, for which a small change (the addition of a small quantity of gas), has a dramatic effect (i.e. substantially reduced drop sizes), even under modest driving pressures (Sovani *et al.* 2001). Its efficiency relies firstly on the change of topology of the liquid in the injection stream resulting from the presence of the bubbles, and secondly on the fast bubble expansion dynamics as the pressure suddenly releases. The coupling between these two effects, along with the associated detailed mechanisms, is still largely unknown.

† Email address for correspondence: h.e.lhuissier@utwente.nl
‡ Also at Institut Universitaire de France.

https://doi.org/10.1017/jfm.2012.481 Published online by Cambridge University Press

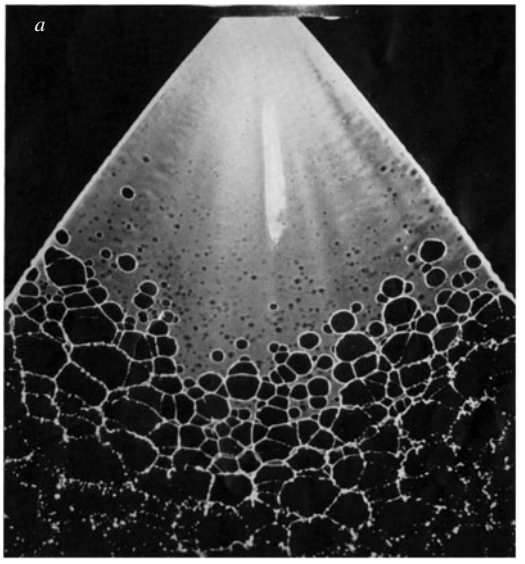


FIGURE 1. (Adapted from figure 28 in Dombrowski & Fraser 1954.) Perpendicular view of a planar sheet formed by injecting an emulsion of oil in water through a fan-spray nozzle. The oil droplets are heterogeneous nucleation sites, and sheet disintegration proceeds from the merging of holes. The image width is 5 cm; see also Rozhkov, Prunet-Foch & Vignes-Adler (2004) for a discrete impact of an emulsion drop on a solid.

Our experimental model, which addresses this problem in two dimensions using a Savart sheet seeded with small air bubbles is itself inspired by a work of Dombrowski & Fraser (1954) using a fan-spray nozzle and a water/oil emulsion (see figure 1). It is representative of the situation of a potential liquid sheet (i.e. with no pre-existing turbulence), which does not flap due to interaction with its environment and which is punctured by holes not too distant from each other (the definition and consequences of 'too distant' will be discussed in § 6). The configuration of a planar circular stationary water sheet seeded with small air bubbles makes visualization possible at every step of the transition from the connected liquid volume to the collection of dispersed drops, and therefore allows for a quantitative description of all those steps. These are as follows, from the centre of the sheet, where the flow is injected, to its periphery where atomization is completed:

(i) the nucleation of holes across the sheet via the bursting of the seeded bubbles;
(ii) the growth of these holes followed by the junction of the rims bordering them into a web of ligaments which concentrates all the liquid injected in the sheet;
(iii) lastly, the breakup of this web into the collection of drops.

A similar effect is obtained by using a mixture of surfactants inducing Marangoni stresses, which eventually puncture the sheet; see Rozhkov, Prunet-Foch & Vignes-Adler (2010) in the context of drop impact. This mechanism is also similar to the spontaneous de-wetting (through hole nucleation, or spinodal decomposition) of a thin film from a solid surface (Reiter 1992) even if it leads to very distinct features of the drop population sizes, as we will see below.

Note that the presence of a dispersed phase within the liquid to atomize is not mandatory for the realization of the first step listed above, that is, the nucleation of

https://doi.org/10.1017/jfm.2012.481 Published online by Cambridge University Press

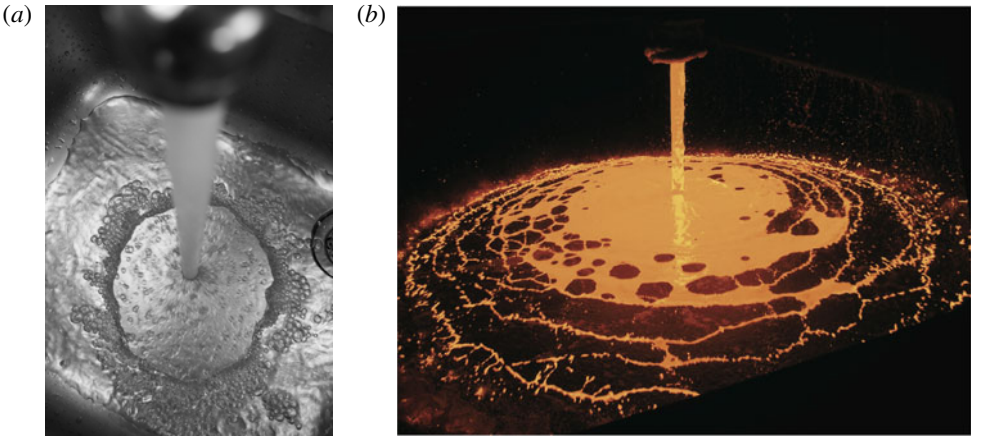


FIGURE 2. (Colour online) (*a*) A tap water jet seeded with small air bubbles by the Venturi air-suction mechanism of the 'aerator'. (*b*) (Adapted from figure 2 in Beskow, Thorén & Lundström 2009.) The Granshot® granulation process (Uddeholm AB Sweden) forming a typical metal 'umbrella'. The iron fragmentation is obtained by the disintegration of a liquid sheet formed by pouring a stream of melt onto a refractory brick (Yule & Dunkley 1994). In contrast to effervescent atomization processes, no secondary phase is dispersed within the liquid to be atomized. Here the holes appear without any nucleation initiator inside the liquid, but probably by droplet projections from the underlying bath dedicated to the quenching of melt droplets. The jet is typically 2 cm in diameter.

holes. The impact of fine droplets of another liquid mediates the nucleation of holes as a result of Marangoni localized stresses (Thoroddsen, Etoh & Takehara 2006). Hole formation on a liquid film may also be the result of an inertial instability, as when the film is violently accelerated perpendicular to its plane, leading to patterns very like those in figure 1 (Bremond & Villermaux 2005). In industrial practice, figure 2(*b*) illustrates that the two former steps leading to the spray are for instance observed in the Granshot® process (Uddeholm AB Sweden), where a single-phase iron melt is fragmented via the disintegration of a planar liquid sheet. This process is a major industrial method for granulation of melts at large output, up to several tons per minute. It is, however, reputed to be '... not very flexible in terms of particle size and shape, these being largely determined by the physical and chemical characteristics of the melt', according to Yule & Dunkley (1994, p. 216), and one could therefore expect 'effervescence' to give more flexibility, if not control, to the process.

After a description of the experimental device and observations (§ 2), the statistical properties of steps (ii) and (iii) above are measured and explained within a geometric model inspired by the kinetics of crystal domain growth (Avrami 1939; Johnson & Mehl 1939). Step (i), concerning the complex interaction of a bubble with the sheet leading to hole nucleation, is not specifically explained here, but is rather taken as an experimental initial condition that we measure, and from which we describe sheet fragmentation. From the observed statistics of nucleation events, the model yields predictions in quantitative agreement with the measurements of the hole size distribution, the sheet's effective radius where disintegration is achieved (§ 3), and the diameters of the liquid ligaments constituting the web (§ 4).

Then the comparison of the distribution of the drop diameters with that of the ligaments of the web reveals that the last step of the atomization process, namely

https://doi.org/10.1017/jfm.2012.481 Published online by Cambridge University Press

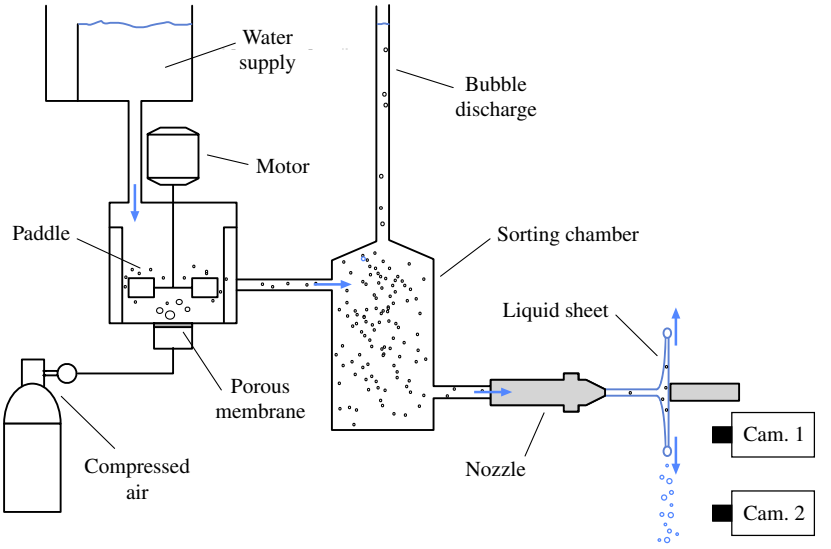


FIGURE 3. (Colour online) Experimental setup for the formation and observation of Savart water sheets seeded with small air bubbles.

the breakup of ligaments, is the one that is responsible for the boardness of the size distribution in the overall spray (§ 5). This *a priori* includes not only the dispersion of drop sizes coming from a single isolated ligament but also the interaction between neighbouring ligaments that are connected at the web nodes. However, we show that the main features of the size distribution in the overall spray can be predicted by considering intra-ligament drop size dispersion alone.

Lastly, the domain of validity of the model we have introduced is discussed in the conclusion (§ 6), together with the distinct breakup mechanisms expected to occur outside this domain.

2. Experimental setup and observations

A smooth, laminar Savart sheet seeded with bubbles is formed according to the experimental setup sketched in figure 3. It has been designed in order to obtain a homogeneous mixture of water and small quasi-mono-disperse air bubbles in large concentration. The dispersion is then injected through a nozzle to form a jet which is shaped into a fluid sheet as it impinges on the solid surface of the impact disk.

2.1. *Experimental setup*

A stationary flow is gravity-driven by the continuous supply of tap water from an elevated tank. The air bubbles are generated in the first chamber in two steps: first, millimetre-sized bubbles are formed by forcing pressurized air through a porous membrane, and second, they are fragmented in order to substantially reduce their size. The fragmentation is achieved by a turbine rapidly rotating in the middle of the chamber. The turbine shape, of Rushton type, and the counter-blades which are fixed to the chamber walls are designed according to a standard protocol to maximize the shear limiting the bubble size (Nagata 1975).

In order to avoid bubble coalescence during this step and after, the bubbles are stabilized by the adjunction of a surface-active component in the water. A commercial

https://doi.org/10.1017/jfm.2012.481 Published online by Cambridge University Press

dish-washing gel (Dreft by Procter and Gamble, which is a mixture of non-ionic and anionic molecules) is incorporated massively in the chamber once and for all at the beginning of each experiment, and the properties of the solution then evolve with the progressive dilution of the initial quantity of surfactant. This evolution proceeds on a characteristic time scale larger than one minute, and for the full time span of a measurement, of the order of one second, the conditions in the Savart sheet can be considered statistically stationary.

The two-phase mixture then transits through a bubble sorting chamber designed to eliminate the largest ones and inject uniform bubble sizes into the sheet. For the bubble diameters $d_b \ll 1$ mm we are concerned with, the bubbles' terminal ascending velocity is prescribed by the dynamic viscosity η of the solution. This velocity is of order $\rho g d_b^2/\eta$, where ρ and g respectively stand for the solution's density and gravity, and it thus depends strongly on the bubble size d_b. By adjusting the height of the sorting chamber outlet pipe with respect to that of the inlet pipe and the time elapsed from the start of bubble production, one can exploit this velocity differential to select a maximal size carried by the slow downward flow in the sorting chamber. It thus permits us to obtain at each moment a narrow bubble size distribution whose mean value evolves slowly during the whole dilution time of the surfactant.

Finally, immediately downstream from the sorting chamber, the mixture is directed to the injector to form a planar liquid sheet homogeneously seeded with the desired small air bubbles. In order to make visualization and lighting easier, the sheet is formed in a vertical plane. The typical velocity in the jet is $u_0 \sim 5$ m s^{-1}, its diameter is $d_0 = 4$ mm and the associated Weber number is $We_0 = \rho u_0^2 d_0/\sigma \sim 10^3$, where σ is the solution's surface tension. The sheets have a radius of $R \sim 10$ cm, and the Froude number $u_0^2/gR > 10$ is thus large enough for gravity to be neglected.

2.2. *Sheet base state*

The two-phase sheet is formed by letting the jet impact on the top of a coaxial solid cylinder, the impact disk (see figure 4). This configuration developed by Savart (1833*a*,*b*) has been preferred to the usual fan-shaped sheets formed by extruding a jet through a slot or cat's-eye-shaped nozzle (e.g. Dombrowski & Fraser 1954) because of the well-controlled axisymmetric properties of the sheet it produces, whose flow and thickness fields are purely radial.

The jet deflection angle at impact is set to $\pi/2$ by adjusting the axial offset of the corona bordering the flat central part of the impact disk: see figure 4 and Clanet & Villermaux (2002). The velocity is thus purely radial at the impact disk edge and a planar liquid sheet is obtained. Since the thickness of the viscous boundary layer on the impact disk $\sqrt{\eta d_d/(\rho u_0)}$ is small compared to the sheet thickness d_0^2/d_d as it leaves the disk in the limit of large jet Reynolds numbers, dissipation in the boundary layer developing over the impact disk is negligible, and the fluid's kinetic energy is conserved during impact. Since, moreover, $u_0^2/gR \gg 1$, this kinetic energy is also conserved all along the sheet, and from continuity equation and symmetry considerations, the thickness h and velocity $\boldsymbol{u}$ are given by

$$\left.\begin{aligned} h &= \frac{d_0^2}{8r}, \\ \boldsymbol{u} &= u_0 \boldsymbol{e}_r, \end{aligned}\right\} \tag{2.1}$$

where r is the radial coordinate as defined in figure 4.

Those base state laws are valid only as long as the sheet is 'intact', or unpunctured by holes, that is to say typically up to the sheet's maximal radial extension in $r = R$.

https://doi.org/10.1017/jfm.2012.481 Published online by Cambridge University Press

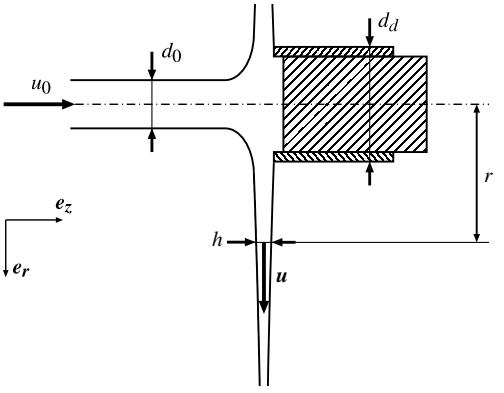


FIGURE 4. Detailed cross-section view of the jet impact. Note the jacket surrounding the solid cylinder, whose axial offset is adjusted in order to ensure a streamline deflection angle of $\pi/2$, to obtain a planar Savart sheet.

When no other disintegration mechanism is involved, R adopts a maximal value L set by the permanent recession of the edge rim at the Culick–Taylor velocity $V = \sqrt{2\sigma/\rho h}$ (Taylor 1959; Culick 1960) at which the radial momentum of the flow is balanced by capillary confinement. The equilibrium radius, where the recession is stationary in the laboratory reference frame, i.e. where $V = u$, is then

$$R = L \equiv \frac{\rho d_0 u_0^2}{16\sigma} d_0 = \frac{We_0}{16} d_0. \tag{2.2}$$

In the present experiments, however, the sheet fragmentation is the consequence of its permanent puncture by the bubbles at radii smaller than L, and the position of its border fluctuates around a mean radius R (typically smaller than L by a factor 2 or 3), which we will determine in terms of the relevant parameters in § 3.2. This behaviour is similar to that observed for large Weber numbers $We_0 \gtrsim 10^3$ (in air) when there are no bubbles dispersed in the liquid: in that case the shear destabilization of the rapidly flowing sheet in the surrounding air at rest provokes sheet fragmentation over a distance smaller than L, decreasing with We_0 (Huang 1970; Villermaux & Clanet 2002; Bremond, Clanet & Villermaux 2007).

2.3. *Bubble sizes and density*

The experiment was not originally designed for the direct measurement of bubble size and density. It is, however, possible to estimate both.

The smallest bubble size is prescribed by the flow around the turbine. Considering the turbine radius $R_T = 3$ cm and its rotation speed $\omega_T \simeq 100\pi$ s^{-1}, the power dissipated by unit of mass is of order $\epsilon \sim \omega_T^3 R_T^2$. Assuming that the typical velocity difference u_ℓ across a distance ℓ in the flow is well represented by Kolmogorov (1941) scaling $u_\ell \sim (\epsilon\,\ell)^{1/3}$, the Weber number of the motion around a bubble of size $d_b = \ell$ is given by

$$We(\ell) = \frac{\rho u_\ell^2 \ell}{\sigma} = \frac{\rho \omega_T^2 R_T^3}{\sigma} \left(\frac{\ell}{R_T}\right)^{5/3}. \tag{2.3}$$

This equation is valid down to the viscous dissipation scale (such that $Re_\ell \sim 1$) of order $R_T\,(\rho R_T^2 \omega_T/\eta)^{-3/4} \approx 1$ μm, a length scale smaller than the bubble size, as will

https://doi.org/10.1017/jfm.2012.481 Published online by Cambridge University Press

be checked *a posteriori*. Considering that a bubble typically fragments as long as the Weber number of the flow at the scale of its diameter d_b is larger than unity (Clay 1940; Hinze 1949; Kolmogorov 1949), the maximal bubble size is then

$$d_b \sim R_T \left(\frac{\rho \omega_T^2 R_T^3}{\sigma} \right)^{-3/5} \simeq 30 \ \mu\text{m}. \tag{2.4}$$

This diameter is of the order of the spatial resolution of our numerical images. The sizes of the smallest bubbles therefore cannot be precisely measured, but we are able to state that all sizes are smaller than 100 μm. The latter are probably of the order of the sheet thickness at the location where the holes form, that is to say from 20 to 40 μm.

The air volume fraction can be estimated via the number of those largest bubbles which are clearly countable in our images, assuming that they concentrate the majority of the air volume. In the regime we studied, their concentration per unit surface of the sheet was between 10^5 and 10^6 m^{-2} for a thickness at the location of the measurements $h \simeq 30$ μm. This gives an air volume fraction in the sheet of

$$\phi_b \sim \frac{d_b^3}{h} \times 10^6 \ \text{m}^{-2} \sim 10^{-4} - 10^{-3}. \tag{2.5}$$

The viscosity (Einstein 1906; Taylor 1932) and density of the solution are therefore those of tap water within relative corrections of order 10^{-3}, which we neglect in the following.

2.4. *Surface tension and hole receding velocity*

As already mentioned, the bubble stabilization requires surfactants to be added to the air/water mixture. The static surface tension of the solution is therefore decreased with respect to the surface tension of tap water. However, because of the large and fast stretching of the fluid elements as they progress radially along the sheet, the surface concentration of the surfactant greatly decreases and the surface tension of pure water is recovered.

Indeed, when a fluid element flows away from the sheet axis it experiences the transverse stretching rate $\partial_t \ln r = u/r$ associated with the radial decay law $h(r) \propto r^{-1}$ of the thickness in (2.1). The area of the fluid element increases at the same rate,

$$\frac{u}{r} > \frac{u}{L} = \frac{16}{We_0} \frac{u}{d_0} \sim 50 \ \text{s}^{-1}, \tag{2.6}$$

which is large compared to the inverse of the typical time scale of diffusion across the film thickness and adsorption at the interface of the surfactant molecules, of order 1 s^{-1} (Couder, Chomaz & Rabaud 1989; Marmottant, Villermaux & Clanet 2000), so that the total surfactant quantity adsorbed at the interface can be considered as constant. The surface concentration is then inversely proportional to the surface area of the fluid element. At a given radius r it is then smaller by a factor of $2r/d_0$ than at the jet surface, and at the sheet edge, for instance, this factor is

$$\frac{2R}{d_0} \sim \frac{2L}{d_0} = \frac{We_0}{8} > 10^2. \tag{2.7}$$

This is clearly larger than the typical dilution factor of a few units, with respect to the maximal compaction of the surfactant molecules adsorbed at the interface, required for surface tension to recover that of pure water (Davies & Rideal 1963). In the spirit of

https://doi.org/10.1017/jfm.2012.481 Published online by Cambridge University Press

Lord Rayleigh (1890) and Bohr (1909) and more recently Marmottant *et al.* (2000), we have checked this assertion experimentally as follows.

Surface tension is measured through the sheet's receding velocity when a hole spontaneously nucleates. In order to limit the influence of the divergence of the streamlines (which are everywhere oriented with the local radial direction $\boldsymbol{e_r}$), we measured the receding velocity at a point where the rim is perpendicular to $\boldsymbol{e_r}$ and is thus precisely progressing in a direction parallel to $\boldsymbol{e_r}$. Also, we minimized the error for the receding velocity due to the sheet thickness gradient by considering only the rim on the side of the hole receding, quasi-stationary against the stream, in the direction $-\boldsymbol{e_r}$, at velocity v_b in the laboratory reference frame. Close to the sheet periphery, this rim recedes over the small distance $v_b\Delta t = (u - V)\Delta t \ll u\Delta t$ for the short duration $\Delta t = 10^{-2}$ s of the measurements, and this recession occurs over a portion of the sheet whose thickness gradient is locally small, i.e. $(d_0/r)^2 \ll 1$. The sheet thickness can thus be considered to be uniform over the region explored by the rim during the measurements, and the actual receding velocity $u - v_b$ we observe can be safely identified with the Taylor–Culick value $V = \sqrt{2\sigma/\rho h}$.

The surface tension $\sigma = \rho h\,(u - v_b)^2\,/2$, estimated by this method over nine independent measurements, is $\sigma = 76$ mN m^{-1}, with a relative standard deviation of 4 %, a value consistent with that known for pure water, $\sigma_{H_2O} = 72$ mN m^{-1} (Lide 1999). It is in any case much larger than the static surface tension $\sigma_{CMC} \simeq 25$ mN m^{-1} of the solution saturated with surfactants, which we measured by the pendant drop method, that is, in the absence of stretching.

3. The holes

Figure 5 shows a typical sheet obtained with the device described above. Close to the axis, the sheet is unpunctured. Then holes nucleate and grow in size, covering an area which increases with the radius r until they all meet and merge to cover the whole available surface at a given radius R. At this radius, the sheet is integrally converted into a two-dimensional web of ligaments. These ligaments then fragment, as seen in figures 6(*a*) and 9, the final collection of drops. With the characterization of this spray of drops as an ultimate goal, we start by describing the hole population and the sheet properties.

3.1. *Hole density and size distribution*

The first step concerns the holes in the sheet. In order to study the holes, the sheet is imaged perpendicularly by a digital fast camera, with a powerful light reflected on the sheet, and a dark background. The holes then appear as dark patches on a shining continuum. The highly contrasted images we obtain are then converted into binary images. By shooting the sheet for a few seconds, its local status (intact or punctured) is detected at every point and for a large number of statistically independent realizations of the same injection conditions. The values we use hereafter are averaged over more than 300 uncorrelated images.

The images are exploited in several ways. The holes' features are first measured through their intersection with line portions drawn at several radii r (see figure 6*a*). The number K of holes cut by unit length of the line and the cord length c of the holes intercepted are measured on each image and for each position of the line. Figures 6(*b*) and 7(*a*) present typical measurements of the mean values $\langle K\rangle$ and $\langle c\rangle$ for the same sheet as a function of the radius r; the averages denoted by $\langle\cdot\rangle$ are taken with respect to time at a fixed radial location.

https://doi.org/10.1017/jfm.2012.481 Published online by Cambridge University Press

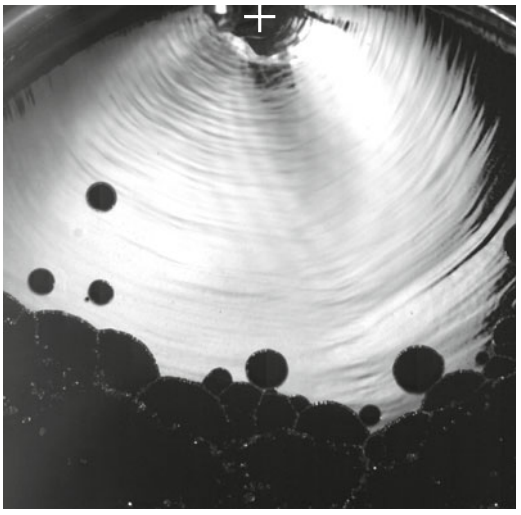


FIGURE 5. Perpendicular view of the two-phase sheet as seen by camera 1 (see figure 3). The axis is indicated by the white cross, the image width is 12 cm and the jet Weber number is $We_0 = 1185$. From the centre at $r = 0$ to its periphery at $r = R$, the sheet is successively: intact, punctured by a few isolated holes, and covered by the merging of the continuously nucleating and growing holes. The liquid of the sheet is then concentrated in a web of ligaments visible at the bottom of the image (see also figures 6(*a*) and 9).

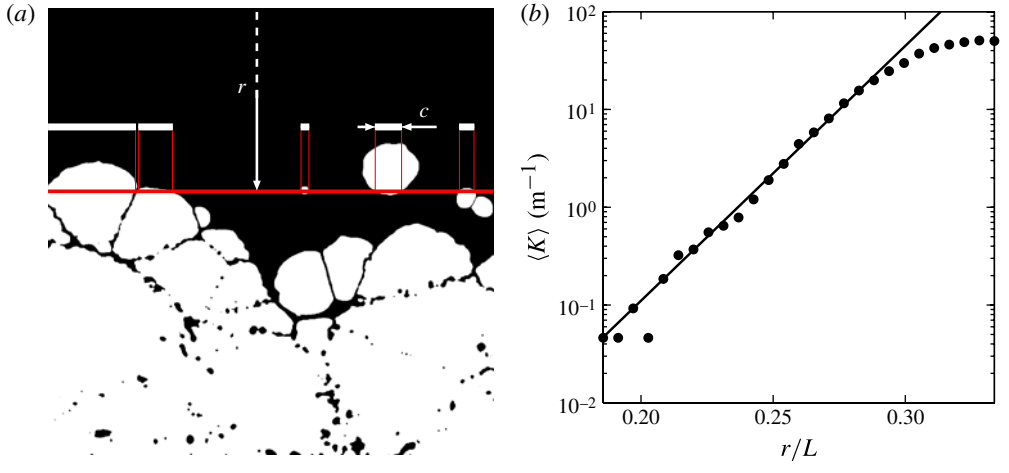


FIGURE 6. (Colour online) (*a*) Measurements of the cord length c defined by the intersection between the holes and a line located at a distance r from the sheet axis. (*b*) Mean lineic density $\langle K \rangle$ of holes intercepted by the line as a function of the line position r (circles) and fit by an exponential $\langle K \rangle = K_0 \, \mathrm{e}^{kr}$ for small r (solid line) (with $K_0 = 68 \times 10^{-8}$ and $k = 60/L \simeq 203$ m^{-1}).

For small radii r, corresponding to the portion of the sheet where the holes do not interact since they are typically too distant from each other, the growth of the mean

https://doi.org/10.1017/jfm.2012.481 Published online by Cambridge University Press

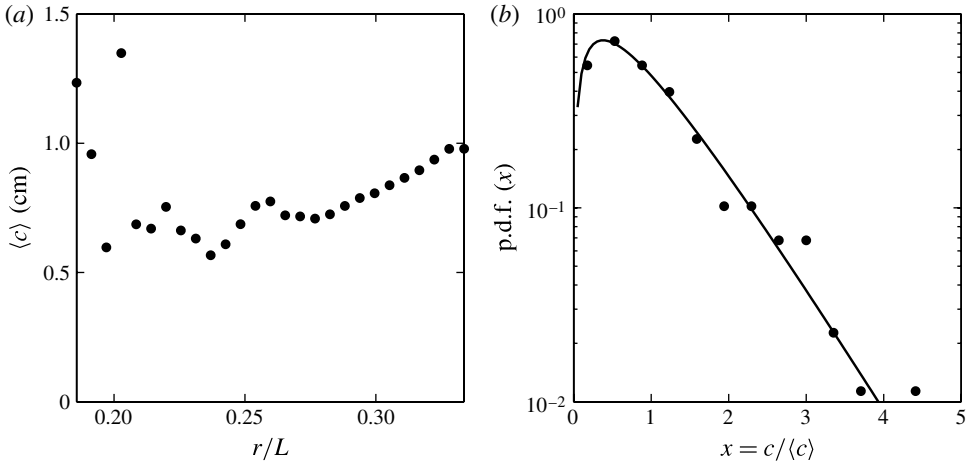


FIGURE 7. (*a*) Mean cord length $\langle c\rangle$ as a function of the radius r for the same sheet as in figure 6. (*b*) Distribution of the cord length c at a fixed radius r (circles) and comparison with distribution (3.10) normalized as $\tilde{\mathfrak{q}}(x) = (\pi^2 x/4)\,\mathrm{K}_0(\pi x/2)$ (solid line).

density $\langle K\rangle$ is exponential, as seen in figure 6(*b*):

$$\langle K\rangle \simeq K_0\,\mathrm{e}^{kr}. \tag{3.1}$$

Since the probability that a circular hole with diameter D is intercepted by an arbitrary line is proportional to D (a big hole is more likely to be cut than a small one), $\langle K\rangle$ is also expressed in terms of the surface concentration of holes Γ by

$$\langle K\rangle = \int_0^\infty \langle\Gamma\rangle D\,\mathfrak{p}(D)\,\mathrm{d}D = \langle\Gamma\rangle\langle D\rangle \tag{3.2}$$

where $\mathfrak{p}(D)$ is the probability density function (p.d.f.) of the hole diameter D.

The variation of the lineic concentration $\langle K\rangle$ with r is thus *a priori* the result of two contributions, namely:

(i) the increase in the surface concentration $\langle\Gamma\rangle$ as new holes appear; and

(ii) the evolution in the mean size $\langle D\rangle$ due to both hole expansion and nucleation of small new holes.

Now figure 7(*a*) shows that the mean cord length $\langle c\rangle$ increases by a factor smaller than 2 only, while $\langle K\rangle$ is multiplied by 10^3. Since for circular holes $\langle c\rangle$ and $\langle D\rangle$ are related by

$$\langle c\rangle = \int_{D=0}^\infty \frac{D}{\langle D\rangle}\,\mathfrak{p}(D)\langle c\rangle|_D\,\mathrm{d}D = \frac{\pi}{4}\frac{\langle D^2\rangle}{\langle D\rangle}, \tag{3.3}$$

where the mean cord length $\langle c\rangle|_D$ inside an isolated hole of diameter D intercepted by an arbitrary line is defined by the p.d.f.

$$\left.\begin{aligned} \mathfrak{q}_D(c) &= \frac{c}{D^2}\,\frac{1}{\sqrt{1-\left(\dfrac{c}{D}\right)^2}}, \\ \langle c\rangle|_D &= \frac{\pi}{4}D. \end{aligned}\right\} \tag{3.4}$$

https://doi.org/10.1017/jfm.2012.481 Published online by Cambridge University Press

Assuming that the shape of the distribution $\mathfrak{p}(D)$ of hole diameters does not evolve radically (which will be checked further), (3.3) implies that $\langle D\rangle \sim \langle c\rangle$, so that $\langle D\rangle$ accordingly increases weakly with r. This means that the increase in $\langle K\rangle$ is essentially due to that in hole concentration $\langle \Gamma\rangle$

$$\frac{\partial\langle K\rangle}{\partial r} \simeq \langle D\rangle \frac{\partial\langle \Gamma\rangle}{\partial r} = \frac{\langle D\rangle}{u}\frac{\mathrm{d}\langle \Gamma\rangle}{\mathrm{d}t} = \frac{\langle D\rangle}{u}\langle f\rangle\,\gamma \tag{3.5}$$

where we have introduced the nucleation rate per unit of time and area γ and the surface fraction f of intact sheet, which by definition satisfies $\mathrm{d}_t\langle \Gamma\rangle = \langle f\rangle\gamma$. This simply means that the holes' density variation in time is the nucleation rate weighted by the sheet fraction which is still intact, since nucleation can only occur on intact portions of the sheet. For small radii $\langle f\rangle \simeq 1$ and then, since $\langle D\rangle$ is essentially constant, one finds from (3.5) that γ is also an exponential function in r:

$$\gamma = \frac{ukK_0}{\langle D\rangle}\,\mathrm{e}^{kr} \equiv \gamma_0\,\mathrm{e}^{kr}. \tag{3.6}$$

Since the holes grow and are advected at constant velocities V and u respectively, the hole size distribution at a given radius r is a consequence of the past 'history' of nucleation events at radii $r' \leqslant r$. A hole having nucleated in r' does indeed have a diameter $D = 2\,(r - r')\,V/u$ once it has been advected down to r, and the p.d.f. in diameters is thus given by

$$\mathfrak{p}(D) = \frac{1}{2V\langle \Gamma\rangle}\,\gamma(r') = \frac{uk}{2V}\,\mathrm{e}^{-(uk/2V)D}, \tag{3.7}$$

where we have considered that the intact fraction $\langle f\rangle \simeq 1$ is essentially constant at small radii so that $u\,\partial_r\langle \Gamma\rangle = \langle f\rangle\gamma \simeq \gamma$. The hole diameters are therefore distributed according to an exponential distribution whose mean $\langle D\rangle = 2V/uk$ is constant, and then (3.3) yields a quantitative prediction for the cords' mean length,

$$\langle c\rangle = \frac{\pi}{2}\langle D\rangle = \pi\frac{V}{uk} \tag{3.8}$$

whose numerical value computed from the independent measurements of u, V and k (shown in figure 6*b*) is

$$\langle c\rangle = 8.5\ \text{mm}. \tag{3.9}$$

This value is in good agreement with the direct measurements reported in figure 7 showing a mean cord length slowly increasing from 6 to 10 mm.

Moreover, the cord length p.d.f. $\mathfrak{q}(c)$ can be inferred from that of the hole diameters D and from the distribution $\mathfrak{q}_D(c)$ of the cord length of an isolated circle with diameter D introduced in (3.4) according to

$$\begin{aligned}\mathfrak{q}(c) &= \int_0^\infty \frac{D}{\langle D\rangle}\,\mathfrak{p}(D)\,\mathfrak{q}_D(c)\,\mathrm{d}D = \frac{c}{\langle D\rangle}\int_0^1 \mathfrak{p}\left(\frac{c}{x}\right)\frac{1}{\sqrt{1-x^2}}\frac{\mathrm{d}x}{x}\\ &= \frac{c}{\langle D\rangle^2}\,\mathrm{K}_0\left(\frac{c}{\langle D\rangle}\right),\end{aligned} \tag{3.10}$$

where K_0 is the modified Bessel function of the second kind and of order zero. This distribution is plotted in figure 7(*b*), where it is seen to compare favourably with the measurements.

https://doi.org/10.1017/jfm.2012.481 Published online by Cambridge University Press

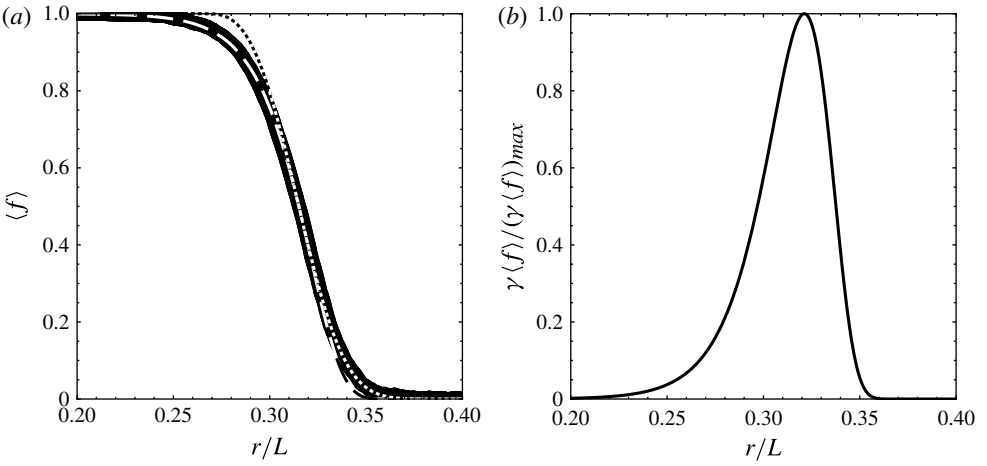


FIGURE 8. (*a*) Surface fraction $\langle f\rangle$ of the sheet that is still intact as a function of the radius r. The average has been taken for more than 300 independent images (circles) and comparison with (3.12) corresponding to an exponential nucleation rate (dashed line). The value of k is independently measured from figure 6(*b*) ($k = 60/L$) and the best fit is obtained for $\mathscr{A} = 2.13 \times 10^{-9}$, which compares favourably with the predicted value $\pi\gamma_0 V^2/(uk)^3 = 2.89 \times 10^{-9}$ of (3.12), determined from independent measurements of u, V, K_0 and k. For comparison, the best fit $\langle f\rangle = \exp[-A\,(r - r_0)^3]$, corresponding to a nucleation rate which would be nil down to r_0 and then constant for $r > r_0$, is also shown (dotted line). (*b*) Effective nucleation rate $\gamma\langle f\rangle$ as a function of r, according to expressions (3.6) and (3.12). The curve is normalized by the maximal value $\gamma_0/2\mathscr{A}\mathrm{e}$ reached in $r = R$.

3.2. *Sheet intact surface and radius*

If the sheet radius R is not well defined instantaneously, as figure 5 illustrates, it is, however, in the mean. In this respect, the fraction f of the sheet that is still intact at a given radius r is the relevant quantity which is the most accessible experimentally. Figure 8(*a*) shows the measurements of the time-averaged fraction $\langle f\rangle$ as a function of r.

This fraction is related to the holes' nucleation rate and opening velocity; $\langle f\rangle$ indeed decreases from 1 to 0 over a distance Δr, which is small compared to the local radius r ($\Delta r/r \simeq 1/3$), and we will consider from now on that the flow velocity $\boldsymbol{u}$ is locally a parallel field (hence disregarding the divergence of the streamlines), and that the holes' opening velocity $V \propto h^{-1/2} \propto r^{1/2}$ is uniform on this portion Δr. As we will see below, this constant opening velocity assumption leads to a good estimate for the sheet radius R. This is probably due to the fact that the slight decrease in the thickness with r is somewhat counterbalanced by the slight decrease in surface tension due to the shrinking of the interfacial area already mentioned at the end of § 2.4.

By definition $\langle f\rangle = 1 - \langle K\rangle\langle c\rangle$, which simply means that the cumulative cut length on a line is the mean cord length times the number of holes. For small radii, that is to say when the holes have not yet merged, the expression for $\langle f\rangle$ can thus be derived on the basis of (3.2) and (3.3) but which are only valid in this restrictive limit ($\langle f\rangle \simeq 1$). However, it is also possible to obtain a more general expression valid for every radius r, even when $\langle f\rangle \ll 1$. In the same way as for the derivation of the distribution in (3.7), this expression involves the history of past nucleation events on an advected portion of the sheet, that is to say nucleation events occurring at smaller radii.

https://doi.org/10.1017/jfm.2012.481 Published online by Cambridge University Press

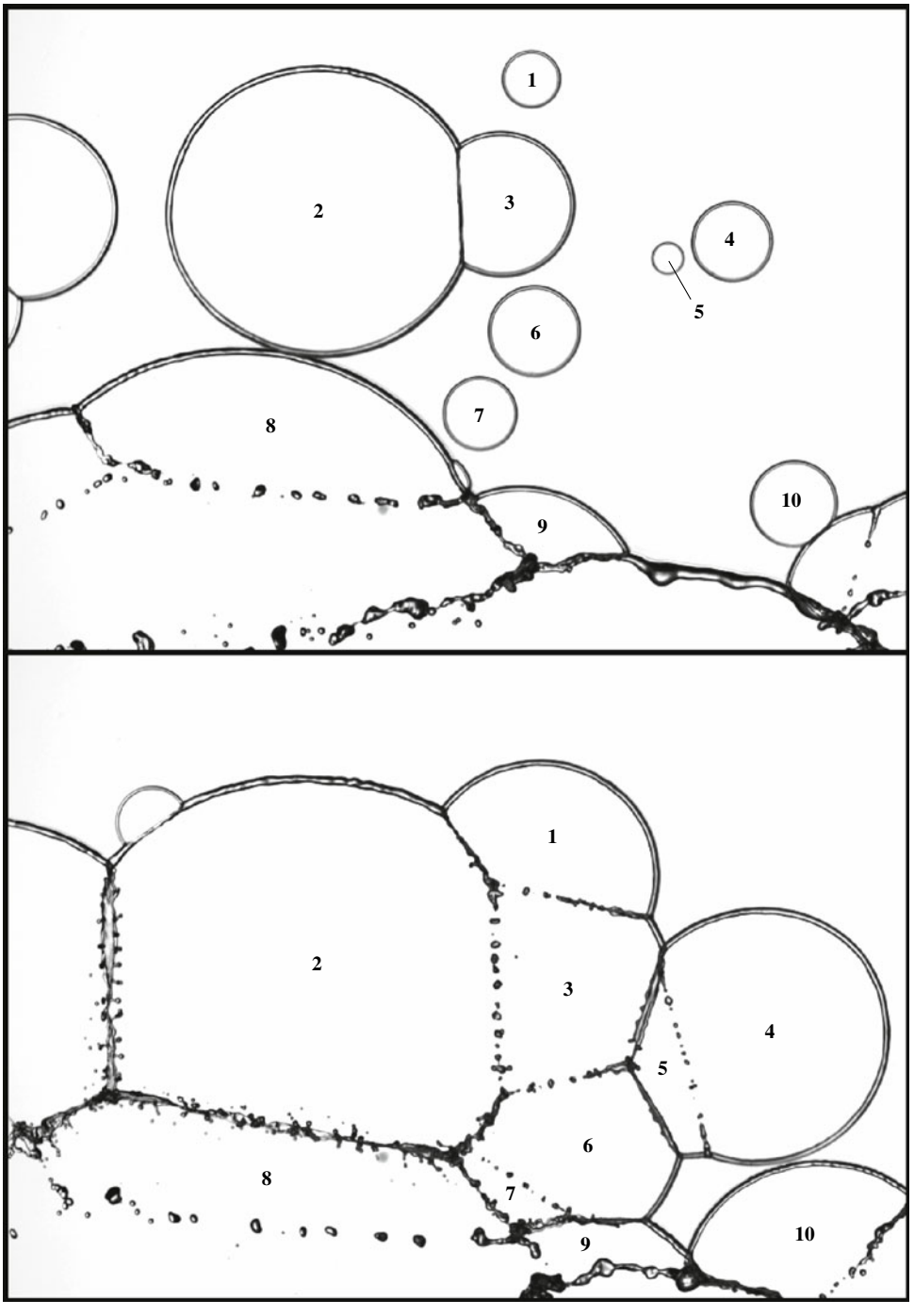


FIGURE 9. Detailed view of the holes' growth, merging and ligament formation. The holes numbered from 1 to 10 grow isotropically while advected by the flow velocity $\boldsymbol{u}$, globally oriented downwards. As their rims join, a web of approximately straight liquid ligaments is formed, which subsequently resolves into a collection of drops. The two images are separated by 2 ms and their width is 50 mm.

https://doi.org/10.1017/jfm.2012.481 Published online by Cambridge University Press

More precisely, the sheet's intact fraction at a given radius r is equal to the probability that an arbitrary sheet portion located in r is not covered by a hole. This is equivalent to saying that, for each of the smaller radii $0 \leqslant r' \leqslant r$ through which the sheet portion has been passing, no hole has nucleated inside a disk $\mathscr{D}$ of radius $V(r-r')/u$ having its centre in r'. Assuming that each of those elementary probabilities associated with a given r' can be written as $\int_{\mathscr{D}} \gamma \, \mathrm{d}\Sigma \, \Delta t' \simeq \gamma(r') \int_{\mathscr{D}} \mathrm{d}\Sigma \, \Delta t'$, that is to say that the effective nucleation rate over the whole disk $\mathscr{D}$ is the same as the nucleation rate in the disk centre in r' (an approach valid as long as $u \gg V$), the intact fraction expected value can be written as a compound Poisson process:

$$\langle f \rangle = \lim_{\Delta t' \to 0} \prod_{t'/\Delta t'=0}^{t/\Delta t'} \left[1 - \pi \frac{V^2}{u^2} (r-r')^2 \, \gamma(r') \Delta t' \right]$$

$$= \mathrm{e}^{-\pi (V^2/u^3) \int_0^r \gamma(r') \, (r-r')^2 \, \mathrm{d}r'}, \tag{3.11}$$

which simply states that $\langle f \rangle$ is the product of the elementary probabilities of non-nucleation for every sheet portion able to propagate a hole down to the location r considered. This result is an extension of those obtained by Johnson & Mehl (1939) for the study of grain boundaries and crystal domains in the context of metal alloy solidification. These authors considered an infinite statistically homogeneous medium and a nucleation rate γ constant in time, and thus obtained in two dimensions $\langle f(t) \rangle_{\boldsymbol{x}} = A \, \mathrm{e}^{-Bt^3}$, which is also presented in figure 8 for comparison. This law is also known as Avrami's equation, since the latter generalized Johnson and Mehl's approach (Avrami 1939, 1940, 1941). Considering an exponential nucleation rate dependence on the radius r, which fits our experiments, $\gamma = \gamma_0 \, \mathrm{e}^{kr}$, (3.11) yields

$$\ln \langle f \rangle = -\mathscr{A} \left[2 \left(\mathrm{e}^{kr} - 1 \right) - kr \left(2 + kr \right) \right], \tag{3.12}$$

where we have introduced the dimensionless quantity $\mathscr{A} \equiv \pi \gamma_0 V^2 / (uk)^3$. A large $\mathscr{A}$ corresponds to an essentially uniform nucleation rate γ over the portion of the sheet that actually experiences nucleation, whereas the small present value $\mathscr{A} \sim 10^{-9}$ expresses a large relative exponential growth over this portion. Equation (3.12) is compared with measurements in figure 8(*a*). Given the approximations used, its agreement is quantitative since the value of $\mathscr{A}$ fitted on the experimental curve is within 30 % of that expected from the independent measurements of the number of holes intercepted by a line (equation (3.6)). Note that the discrepancy in R corresponding to those 30 % on $\mathscr{A}$ is less than 2 %.

The sheet's effective radius R is straightforward to derive from (3.12). It corresponds to the sharp transition between the intact and disintegrated portions of the sheet, at which the fraction $\langle f \rangle$ suddenly decreases from 1 to 0. Using the fact that at this transition $\mathrm{e}^{kr} \gg kr$, since $kr \simeq 20$, the radius R can be defined as the location where $\ln \langle f \rangle \sim -1$, that is to say

$$R \simeq -\frac{\ln(2\mathscr{A})}{k}, \tag{3.13}$$

whose numerical value for the sheet in figure 8 is $R = 0.32L$. Note that although the criterion on $\langle f \rangle$ is somewhat loosely defined, the radius R is nevertheless accurately determined owing to the strong dependence of $\langle f \rangle \sim \exp[-2\mathscr{A} \exp(kr)]$ on r for large kr.

https://doi.org/10.1017/jfm.2012.481 Published online by Cambridge University Press

3.3. *Hole surface concentration*

An essential feature of the ligament web formed at the sheet periphery is the ultimate average size of the holes, or alternatively the average distance separating their centres. This is given by the terminal surface concentration Γ_∞ of the holes when they have all joined. It is indeed the latter that sets the typical size of the holes and therefore, by interstitial liquid conservation, that of the ligaments from which the drops are generated.

By definition, Γ_∞ is the sum (by unit of area) of the number of holes nucleated at every radial location r on a sheet portion flowing at a constant radial velocity u, that is to say

$$\Gamma_\infty = \int_0^\infty \gamma\, \langle f \rangle \, \mathrm{d}t = \int_0^\infty \gamma\, \langle f \rangle \, \frac{\mathrm{d}r}{u}. \tag{3.14}$$

If the exponential law for the nucleation rate (3.6) is typically valid down to R, an expression for Γ_∞ can be obtained, once again making use of $\mathrm{e}^{kR} \gg kR$, given by

$$\Gamma_\infty \simeq \frac{\gamma_0}{u} \int_0^\infty \mathrm{e}^{kr - \mathscr{A}\,\mathrm{e}^{kr}}\, \mathrm{d}r = \frac{\gamma_0}{uk}\, \frac{\mathrm{e}^{-\mathscr{A}}}{\mathscr{A}}. \tag{3.15}$$

For comparison, the case where the nucleation rate γ and the opening velocity V are both uniform over the sheet would yield $\Gamma_\infty = \int_0^\infty \gamma \langle f \rangle \, \mathrm{d}t = \Gamma(4/3)\, (3\gamma^2/\pi V^2)^{1/3}$, where

$$\Gamma(x) = \int_0^\infty t^{x-1} \mathrm{e}^{-t}\, \mathrm{d}t \tag{3.16}$$

is the Gamma function.

For the case under consideration here, (3.15) yields numerically

$$\Gamma_\infty = 4.4 \times 10^4 \ \mathrm{m}^{-2} \tag{3.17}$$

which, after comparison with the estimate in § 2.3 for the bubble density, means that approximately 1/10th of the bubbles actually nucleate a hole. This behaviour is consistent with two direct observations.

(i) Bubbles can burst without necessarily nucleating a growing hole (because it was initially too small (Taylor & Michael 1973), or because only one of the two liquid lamellas separating the bubble cavity from the atmosphere actually punctured), as shown by radially expanding surface waves originating from a point of the sheet observed from time to time.

(i) The majority of the bubbles are collected into a rim before bursting and having the opportunity to generate a hole.

4. The web of ligaments

When a hole nucleates and grows, the liquid formerly constituting the sheet is collected into a toroidal rim at the border of the hole. In the present context where numerous holes nucleate close to each other within a short time lapse, the holes extend until they merge by impingement of their rims, thus realizing a tessellation of the sheet plane. At that instant in time, the rims from all the adjacent holes have joined to form a web of liquid ligaments, which subsequently fragment to produce the spray of drops, as figure 9 illustrates. Since we want to describe the drop content of the spray,

https://doi.org/10.1017/jfm.2012.481 Published online by Cambridge University Press

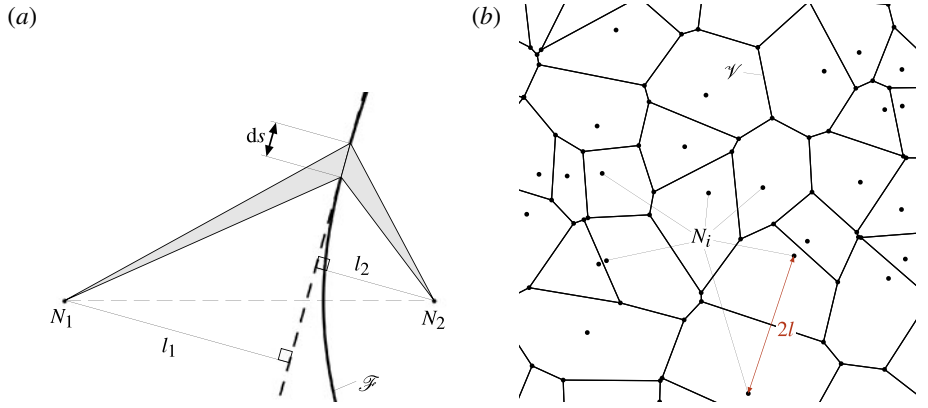


FIGURE 10. (Colour online) (*a*) Portion of a liquid ligament $\mathscr{F}$ constituting the border between two adjacent holes having nucleated at the points N_1 and N_2 at different instants in time: $\mathscr{F}$ is then an arc of a hyperbola (nucleation in N_1 occurred prior to that in N_2 in this example). The liquid quantity per unit of length of the ligament is proportional to the grey area divided by ds, i.e. to the sum $(l_1+l_2)/2$ in expression (4.1). For a synchronous nucleation, $\mathscr{F}$ lies on the bisecting line of N_1N_2 and then $l_1 = l_2 = l$ all over the ligament length, which thus has a uniform section. (*b*) Example of a Voronoï diagram $\mathscr{V}$ associated with the points N_i randomly distributed over the plane. It coincides with the web of liquid ligaments for holes nucleating synchronously at those points N_i.

it is thus mandatory to characterize the statistical properties of this web in order to understand those of the final collection of drops.

The question here is to determine the cumulative length (per unit area of the sheet) of the ligaments having a given size, i.e. whose diameter lies between d_l and $d_l + \mathrm{d}d_l$. Since the ligaments concentrate the liquid which was initially 'filling' the holes, the diameter of a ligament portion is, by mass conservation, simply given by (see figure 10)

$$d_l = \sqrt{\frac{2h(l_1 + l_2)}{\pi}}, \tag{4.1}$$

where one sees that the relevant lengths are the normal distances l_1 and l_2 from the ligament tangent line to the two nucleation sites it separates. This geometric constraint directly gives the characteristic scaling $d_l \sim \sqrt{\langle l \rangle h}$ for the diameter of the ligaments.

In the general case where nucleation is a Poisson process both in space and time (i.e. when the probability of nucleation over a small surface of area dΣ during a small time interval dt is directly proportional to dΣdt: see (3.11)), computing the distribution of d_l is difficult. The only known analytical results concern the one-dimensional problem; that is to say the growth, from nucleation sites randomly distributed on a line, of segments whose frontiers amount to single points (Johnson & Mehl 1939; Meijering 1953). In two dimensions the hole borders, i.e. the web of ligaments, are composed of portions of hyperbolas, making the analysis complicated.

This is not, however, a big limitation on the description of the present problem. Indeed, the nucleation on the advected sheet occurs within a very short time interval (i.e. nucleation mainly occurs around a given radius of the sheet) compared to the

https://doi.org/10.1017/jfm.2012.481 Published online by Cambridge University Press

holes' growth time, of order $\Gamma_\infty^{-1/2}/V$. This assumption is not exactly satisfied, since if the nucleation is indeed well concentrated around a particular radius of the sheet as figure 8 emphasizes, the hole diameters (which all open at the same velocity) are nevertheless clearly distributed at a given radial location, as we saw in § 3.1. This simplifying assumption has the great advantage of being exactly solvable, and hence physically transparent. It is particularly relevant to illustrating the role played by web geometry in drop size distribution, as will be seen below. We will also demonstrate that a more sophisticated model accounting for the spreading of nucleation times is unnecessary, since the spray features will be shown to be dominated by other effects, as discussed in § 5.3.

The limit case we study is the one where all the holes appear at the same moment and nucleation is considered as a Poisson process in space only; that is to say that the nucleation probability over an infinitesimal surface of area $\mathrm{d}\Sigma$ only depends on $\mathrm{d}\Sigma$ and can be written as $\beta\,\mathrm{d}\Sigma$, where β is a nucleation probability per unit area (β is equivalently the mean hole surface density and for comparison with experiments in § 5.1 it will be identified with the terminal density Γ_∞). The ligament web is then the set $\mathscr{V}$ of the edges of the Voronoï polygons, or cells, associated with the nucleation sites, where the Voronoï cell associated with a nucleation site N is the set of every points in the plane which are closer to N than to any other nucleation site (see figure 10). Even in this simple case, analytical results are scarce. Only the means and possibly the first moments of the distributions of area, perimeter or number of edges of the polygons are known (Santaló 2004).

However, the p.d.f. of the normal distances l can be derived analytically (our original derivation is presented in § A.1), and is found to be a Rayleigh distribution:

$$\left.\begin{aligned} \tilde{\mathfrak{r}}\left(\tilde{l}\equiv\frac{l}{\langle l\rangle}\right)&=\frac{\pi}{2}\tilde{l}\,\mathrm{e}^{-\pi\tilde{l}^2/4},\\ \langle l\rangle&=\frac{\beta^{-1/2}}{2}, \end{aligned}\right\} \tag{4.2}$$

where $\mathfrak{r}(l)$ denotes the probability density that a ligament portion of infinitesimal length $\mathrm{d}s$ taken randomly on the ligament web is at a distance l from the closer nucleation site (in other words it is the expected portion of the perimeter of a cell that is at a normal distance l from its centre).

In addition to this distribution, the total length $\mathscr{L}$ of the web ligaments per unit area of the sheet is known (see § A.1). It is expressed as the product of half the mean perimeter of a hole $\langle P\rangle/2 = 4\beta^{-1/2}/2$ (since every ligament is shared by two holes) by the holes' surface concentration β, i.e.

$$\mathscr{L}=2\sqrt{\beta}. \tag{4.3}$$

Since in the case of a synchronous nucleation the ligament web is the Voronoï diagram of the nucleation sites, we have $l_1 = l_2 = l$ (every ligament is equidistant from its two neighbouring nucleation sites), and thus (4.1) amounts to

$$d_l=\sqrt{4lh/\pi}. \tag{4.4}$$

The p.d.f. of ligament diameters d_l (still relative to a ligament portion of fixed infinitesimal length $\mathrm{d}s$) is then directly derived from that of the lengths l, and is

https://doi.org/10.1017/jfm.2012.481 Published online by Cambridge University Press

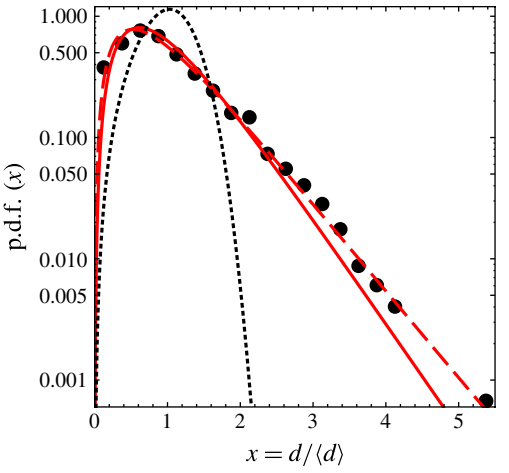


FIGURE 11. (Colour online) Normalized probability density of drop diameters d measured downwards from the sheet edge (i.e. in $r > R$) for more than 6000 drops (circles) with mean value $\langle d\rangle = 0.60$ mm. Comparison with the normalized distribution $\tilde{\mathfrak{u}}_n(\tilde{d})$ from (5.15) plotted for the experimental value $n = 4$ measured in figure 13 (solid line) and for the best fit value $n = 3$ (dashed line). The distribution $\tilde{\mathfrak{u}}_\infty(\tilde{d})$ defined in (5.4) and resulting from a mono-disperse ligament breakup is also plotted (dotted line) for comparison.

given by

$$\left.\begin{aligned} \tilde{\mathfrak{s}}\left(\tilde{d}_l \equiv \frac{d_l}{\langle d_l\rangle}\right) &= 4\Gamma\left(\frac{5}{4}\right)^4 \tilde{d}_l^{\,3}\, \mathrm{e}^{-[\Gamma(5/4)\tilde{d}_l]^4}, \\ \langle d_l\rangle &= \frac{2\sqrt{2}}{\pi^{3/4}}\,\Gamma\left(\frac{5}{4}\right)\sqrt{\langle l\rangle h}. \end{aligned}\right\} \tag{4.5}$$

This is a distribution highly concentrated around its mean, the reasons for this being first the nonlinear transformation involving a square root in (4.4), and second that ligaments are built by an averaging interaction of adjacent hole rims, thus averaging out the disorder induced by the Poisson hole nucleation process. The consequences of this concentration will be clarified in the next section.

5. The drops

We finally turn to the distribution of drop diameters d in the overall spray resulting from the fragmentation of the ligament web. Experimentally, at the same time that the sheet and the holes are imaged with a first camera, as described above, the drops are recorded with a second camera located sufficiently far radially (see figure 3) for them to have enough time to relax to a spherical shape. The depth of field is deliberately reduced, and the focus plane is adjusted to coincide with that of the sheet; only those drops in focus and having a sharp contour are processed further.

A typical drop diameter distribution is presented in figure 11. It arises from the sheet on which the measurements of the previous section have been made. The ligaments constituting the web break up via a more or less noisy Plateau–Rayleigh mechanism owing to their more or less corrugated cylindrical geometry. We describe

https://doi.org/10.1017/jfm.2012.481 Published online by Cambridge University Press

below step by step the relative importance of the factors determining the overall drop size distribution.

5.1. *The geometric contribution of the ligament web*

For an smooth and infinite ligament having a uniform cylindrical section with diameter d_l, the fastest growing wavelength of the instability is (Lord Rayleigh 1878)

$$\lambda_\infty \simeq 4.51\, d_l, \tag{5.1}$$

thus defining a unique drop size $\langle d\rangle|_{d_l}$.

As a first step, it is instructive to disregard both the influence of the web nodes (at the junction of three ligaments) and that of the drop size dispersion from single ligament breakup (the size distribution around $\langle d\rangle|_{d_l}$), to only consider the contribution of the ligament web geometry itself, namely the distribution of d_l. This gives rise to a trivial mono-disperse ligament p.d.f. $\mathfrak{t}_\infty$ for the ratio of the drop diameters d to the ligament diameter d_l from which they originate:

$$\left.\begin{aligned} \mathfrak{t}_\infty\left(\frac{d}{d_l}\right) &= \frac{1}{b_\infty}\,\delta\left(\frac{d}{d_l} - b_\infty\right), \\ b_\infty &= \frac{\langle d\rangle|_{d_l}}{d_l} = \left(\frac{3}{2}\frac{\lambda_\infty}{d_l}\right)^{1/3} \simeq 1.89, \end{aligned}\right\} \tag{5.2}$$

where δ denotes the Dirac delta function.

The overall spray drop size dispersion in this idealized sketch is then written as the average of the mono-disperse drop size distributions $\mathfrak{t}_\infty$ from each ligament weighted by the distribution $\mathfrak{s}$ of the ligament sizes in the web and the number of drops per ligament length:

$$\begin{aligned} \mathfrak{u}_\infty(d) &\propto \int_0^\infty \frac{1}{\langle d\rangle|_{d_l}}\,\mathfrak{t}_\infty\left(\frac{d}{d_l}\right)\mathfrak{s}(d_l)\,\frac{\partial(d/d_l)}{\partial d}\,\mathrm{d}d_l \\ &\propto \int_0^\infty \frac{1}{d_l}\,\mathfrak{t}_\infty\left(\frac{d}{d_l}\right)\mathfrak{s}(d_l)\,\frac{1}{d_l}\,\mathrm{d}d_l \end{aligned} \tag{5.3}$$

(this average obviously amounts to a simple variable substitution due to the Dirac delta function in $\mathfrak{t}_\infty$, but we keep this formalism for consistency of presentation, anticipating its necessary use in § 5.3). Here the first factor $(\langle d\rangle|_{d_l})^{-1} \propto d_l^{-1}$, which weights the distribution $\mathfrak{t}_\infty(d/d_l)$ in the integrand, accounts for the number of drops per ligament length, which has to be considered since the distribution $\mathfrak{s}(d_l) = \tilde{\mathfrak{s}}(\tilde{d}_l)/\langle d_l\rangle$ precisely refers to the probability that a given elementary length of ligament has diameter d_l, whereas the second factor d_l^{-1} simply arises from the variable substitution. The corresponding normalized drop size distribution is then given by

$$\left.\begin{aligned} \tilde{\mathfrak{u}}_\infty\left(\tilde{d} \equiv \frac{d}{\langle d\rangle_\infty}\right) &= \frac{4\,\tilde{d}^2}{\Gamma\left(\frac{3}{4}\right)^4}\,\mathrm{e}^{-[\tilde{d}/\,\Gamma(3/4)]^4}, \\ \langle d\rangle_\infty &= \frac{2\sqrt{2}\,b_\infty}{\pi^{3/4}\Gamma\left(\frac{3}{4}\right)}\,\sqrt{\langle l\rangle h}. \end{aligned}\right\} \tag{5.4}$$

As expected, this idealized limit provides a poor description of the spray drops, as can be seen in figure 11. The true distribution is much broader, and skewed towards

https://doi.org/10.1017/jfm.2012.481 Published online by Cambridge University Press

the large drop sizes, a feature this geometric limit does not account for. At best, this scenario gives an order of magnitude of the average drop size $\langle d\rangle$. Indeed, the Voronoï web, from which the ligament length distribution (4.2) and therefore (5.4) have been derived, has to be attributed the same hole surface concentration as that of the true sheet, that is to say $\beta = \Gamma_\infty$, where Γ_∞ is the terminal value we determined in § 3.3 in terms of the measured nucleation rate. This yields

$$\langle d\rangle_\infty = \frac{2\sqrt{2}\, b_\infty}{\pi^{3/4}\Gamma\left(\frac{3}{4}\right)}\sqrt{\frac{h}{2\Gamma_\infty^{1/2}}} \simeq 1.31\sqrt{\frac{h}{\Gamma_\infty^{1/2}}}, \tag{5.5}$$

whose numerical value for the example we have been studying from the beginning is $\langle d\rangle_\infty = 0.43$ mm. This value is 30 % off the experimental one directly measured from the drop population $\langle d\rangle = 0.60$ mm. This is not surprising given that the purely geometric description of distribution (5.4) disregards the possible aggregation phenomena resulting from the capillary interaction between the ligaments at their merging nodes, and those peculiar to the ligament dynamics itself, both effects which tend to increase drop size, and which we consider in the next section.

In order to appreciate the efficiency of the 'effervescent' process, this value for the mean drop size when bubbles are puncturing the sheet has to be compared with that obtained when there is no bubble in the water flow. For working conditions ($We_0 \simeq 1200$ and for two different jet diameters $d_0 = 2.7$ mm and $d_0 = 5$ mm) very similar to the one for which we measure $\langle d\rangle = 0.60$ mm ($We_0 = 1185$ and $d_0 = 4$ mm), Clanet & Villermaux (2002) measured a much larger value $\langle d\rangle \simeq 2.2$ mm. This decrease in the drop size by a factor larger than three illustrates the strong impact of the very small air fraction we introduced into the sheet on its fragmentation.

5.2. *The contribution of the web nodes*

The influence of the web nodes, which we have so far neglected, on the overall spray can be estimated by comparing the number of drops originating from the edges of the web themselves (the ligaments) with the number of drops originating from the nodes of the web (both per unit area of the sheet), as shown in figure 12. According to § 5.1, the former is the total length of the ligaments divided by the mean drop size

$$\Gamma_L = \frac{\mathscr{L}}{\langle d\rangle_\infty} \simeq 1.53\beta^{3/4}\, h^{-1/2}, \tag{5.6}$$

where 'L' stands for ligament. On the other hand the latter, Γ_N (where 'N' stands for node), results from the density of cells β, assuming simply that each node gives rise to a single drop,

$$\Gamma_N = \frac{\langle \nu\rangle}{3}\beta = 2\beta, \tag{5.7}$$

where $\langle \nu\rangle = 6$ is the mean number of nodes per cell and 3 is the number of cells per node, as expected from the Descartes–Euler theorem relating the total number of cells, edges and nodes in any tessellation of the infinite plane.

The ratio Γ_N/Γ_L of the two densities is of order $(\beta h^2)^{1/4}$, exhibiting a weak dependence on the dimensionless hole surface density βh^2. In the present case

$$\beta h^2 \equiv \Gamma_\infty h^2 \simeq 2.2\times 10^{-5}, \tag{5.8}$$

https://doi.org/10.1017/jfm.2012.481 Published online by Cambridge University Press

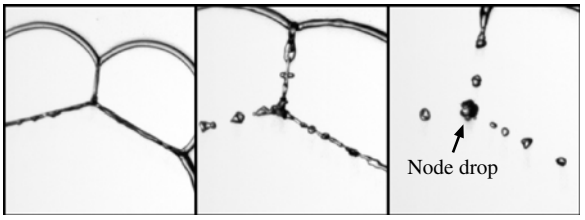


FIGURE 12. Example of a node drop. The images are 8.6 mm wide and are spaced by 1 ms.

and therefore

$$\frac{\Gamma_N}{\Gamma_L} \simeq 9\,\%. \tag{5.9}$$

The contribution of the node drops is thus small, but not negligible and, depending on the way they are distributed in size, could interfere with the large excursion tail of the overall drop size distribution.

The node drop size distribution is, however, very narrow, as simple geometric considerations show. Assuming that the diameter d of each node drop is given by the liquid contained in the three rim portions (from each adjacent hole), connected at the node by capillarity by a bridge of length d, we have $4\pi\,(d/2)^3\,/3 = 3 \times qdh/2$ and the node drop diameter is given by

$$d = \sqrt{\frac{9qh}{\pi}}, \tag{5.10}$$

where q is the distance from the node to the nucleation sites (see figure 16 in § A.2). The dispersion in d is therefore just a consequence of that in q. Since the latter is given by the narrow distribution $\mathfrak{v}(q)$ found by Meijering (1953), and which we briefly re-establish in § A.2,

$$\left.\begin{aligned} \mathfrak{v}(q) &= 2\,(\pi\beta)^2\; q^3\,\mathrm{e}^{-\pi\beta q^2}, \\ \langle q\rangle &= \tfrac{3}{4}\beta^{-1/2}, \end{aligned}\right\} \tag{5.11}$$

the distribution of the node drop diameters d is given by

$$\left.\begin{aligned} \mathfrak{w}(d) &= \mathfrak{v}(q)\frac{\partial q}{\partial d} \sim \frac{\beta^2}{h^4} d^7\,\mathrm{e}^{-\beta d^4/h^2}, \\ \langle d\rangle|_N &= \frac{7}{4}\frac{\Gamma\left(\dfrac{3}{4}\right)}{\pi^{3/4}}\sqrt{\frac{h}{\Gamma_\infty^{1/2}}} \simeq 1.44\sqrt{\frac{h}{\Gamma_\infty^{1/2}}}, \end{aligned}\right\} \tag{5.12}$$

which, not surprisingly, is even narrower than the distribution $\tilde{\mathfrak{u}}_\infty(d)$ of the drops resulting from the ligaments assumed to break in a mono-disperse fashion. The reason is that the distances q to a node, having three equidistant nucleation sites, are more constrained than the normal distances to an edge segment l, having only two equidistant nucleation sites, and therefore their distribution $\mathfrak{v}(q)$ is less dispersed than $\mathfrak{r}(l)$.

The mean node drop size $\langle d\rangle|_N$, in addition, is almost coincident with that of the drops $\langle d\rangle_\infty$ resulting from the mono-disperse breakup of the ligaments ($\langle d\rangle|_N/\langle d\rangle_\infty \simeq 1.10$). The overall drop size distribution accounting for the contribution of both

https://doi.org/10.1017/jfm.2012.481 Published online by Cambridge University Press

ligament and node drops that could be obtained by composing the corresponding distributions $\mathfrak{u}_\infty(d)$ and $\mathfrak{w}(d)$, weighted by Γ_L and Γ_N respectively, thus has no way to match or even approach the experimental distribution in figure 11, and especially to account for its broad tail.

The analysis above shows that even by considering the nodes of the ligament web, the conclusion at the end of § 5.1 remains unchanged: the drop size dispersion in the spray cannot be explained on the basis of a purely geometric representation of a web of ligaments, each breaking into a single-sized population of drops. The ligament dynamics itself has to be considered.

5.3. *Dispersion within each ligament*

The discrepancy in the drop size distributions between the geometric model of §§ 5.1 and 5.2 and experiments cannot be attributed to the simplifications we made to the web geometry when assimilating it to a Voronoï diagram rather than to the complex web of hyperbola arcs one would have expected for a nucleation process distributed in time (or equivalently spatially distributed along the sheet radius). Indeed, in this case the distances l_1 and l_2 covered by two rims joining to form a ligament are no longer necessarily equal (see figure 10). Since the cross-section area $\pi d_l^2/4$ of the resulting ligament is proportional to the sum $l_1 + l_2$, its p.d.f. is written as the self-convolution of that of the individual distances l, and it is then necessarily narrower. Similarly, the distribution of d_l is necessarily narrower than that of d_l^2. Therefore, all the ingredients responsible for the narrowness of $\tilde{\mathfrak{s}}(\tilde{d}_l)$ are expected to also be present in a model where nucleation would be distributed in time. Assuming synchronous nucleation is thus not a big issue.

The clear difference between the measurements in figure 11 and expression (5.4) for $\mathfrak{u}_\infty(d)$ singles out, on the contrary, the decisive importance of the intrinsic ligament dynamics on the drop production process. Ligaments as they break through a noisy process due to their corrugation do indeed produce a broad collection of sizes; also, ligaments interact with their neighbours via their connecting node. Direct observation indicates that the nodes in the web (at the junction of a ligament triplet) are the source of the largest drops. During the breakup period $(\rho d_l^3/\sigma)^{1/2}$, the ligaments connected by their extremities partially empty into each other via the nodes. The draining direction is imposed by the difference of capillary pressure $2\sigma/d_l$ between the connected ligaments. By this mechanism, the thinner ligaments empty into the thicker ones and become thinner, thus enhancing the pre-existing dispersion resulting from the geometric distribution of the distances l. A similar mechanism is at play during the breakup of a ligament with an initial irregular cross-section.

Having these effects in mind, we now show that a fairly accurate representation of the experimental data can be derived on the basis of the ligament web characteristics we derived in § 4 by simply taking into account the dispersion of drop sizes within each ligament. Indeed, the drop size dispersion intrinsic to the breakup of an isolated ligament is usually well described by a gamma distribution extending around the mean size $\langle d\rangle|_{d_l}$ (Villermaux, Marmottant & Duplat 2004; Bremond & Villermaux 2006)

$$\tilde{\mathfrak{g}}_n\left(x = \frac{d}{\langle d\rangle|_{d_l}}\right) = \frac{n^n}{\Gamma(n)}\, x^{n-1}\, \mathrm{e}^{-nx}, \tag{5.13}$$

whose parameter n setting the width of the distribution depends on the corrugation of the source ligament prior to breakup. A smooth ligament has a large n with a narrow distribution around the mean (that limit would correspond to the picture

https://doi.org/10.1017/jfm.2012.481 Published online by Cambridge University Press

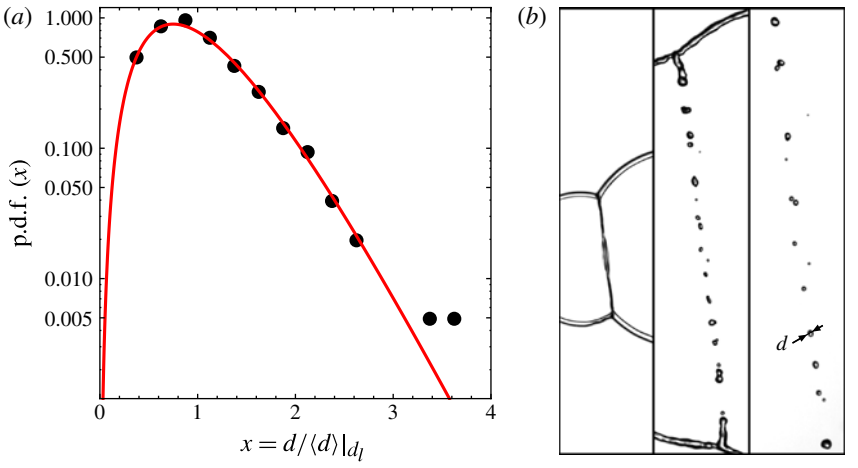


FIGURE 13. (Colour online) (*a*) Probability density function of drop sizes $d/\langle d\rangle|_{d_l}$ relative to their mean diameter $\langle d\rangle|_{d_l}$ for each ligament, averaged over a set of 64 independent and randomly selected ligaments totalling 820 drops (circles). The gamma distribution $\tilde{\mathfrak{g}}_n(\tilde{d})$ as defined in (5.13) is plotted with $n = 4$ (solid line). (*b*) Example of ligament breakup. The intra-ligament drop size dispersion is obvious in the last image. The image height is 24 mm, and time between images is 1/500 s.

in (5.2)). Conversely, a ligament initially strongly corrugated by large-amplitude random capillary waves has a small n and produces a broad collection of drop sizes.

This general picture is also relevant to the present context: we took measurements of the size dispersion among several drop populations, each coming from a given ligament. The fragmentation products of more than 60 randomly selected ligaments was thus documented. For each ligament the sizes d of the resulting drops were measured and made dimensionless by their mean size $\langle d\rangle|_{d_l}$. The distribution obtained for the relative size $d/\langle d\rangle|_{d_l}$ of all the drops from all the ligaments is plotted in figure 13. It is very well described by a gamma distribution of order $n = 4$.

This particularly small order ($n = 4$) is consistent with the fact that ligaments are formed by the inelastic collision of two rapidly receding rims (see for instance figure 9), which may even lead to their destruction, a point we return to below. Before being dissipated, the incident kinetic energy of the rims produces irregular motion within the ligaments, whose surface is thus rough. The corresponding drops after breakup are consequently broadly dispersed (the scaled standard deviation is 1/2).

Building on the experimental determination of this intermediate distribution, which offers an accurate description of the drop size dispersion for a large number of ligaments with various diameters, we now derive a realistic expression for the drop size distribution for the whole fragmentation process. Indeed, the distribution of the drop diameter d resulting from the breakup of a single isolated ligament of diameter d_l is obtained from the normalized (5.13),

$$\mathfrak{t}_n\left(\frac{d}{d_l}\right) = \frac{1}{b_n}\,\tilde{\mathfrak{g}}_n\left(\frac{d}{b_n d_l}\right), \tag{5.14}$$

where b_n is the mean value of $\mathfrak{t}_n$, that is to say $b_n = \langle d\rangle|_{d_l}/d_l$ is the ratio of the mean diameter $\langle d\rangle|_{d_l}$ of the drops resulting from a single ligament to its diameter d_l. In the limit $n \to \infty$, (5.2) for a mono-disperse drop distribution is recovered.

https://doi.org/10.1017/jfm.2012.481 Published online by Cambridge University Press

The distribution for the drop diameters d in the whole spray is then simply expressed (as in equation (5.3)) as the sum of the ligaments' weighted contributions,

$$\mathfrak{u}_n(d) \propto \int_0^\infty \frac{1}{d_l}\,\mathfrak{t}_n\left(\frac{d}{d_l}\right)\,\mathfrak{s}(d_l)\,\frac{1}{d_l}\,\mathrm{d}d_l, \tag{5.15}$$

yielding the mean drop size

$$\langle d\rangle_n = \frac{n}{n-1}\,\frac{2\sqrt{2}\,b_n}{\pi^{3/4}\Gamma\left(\dfrac{3}{4}\right)}\,\sqrt{\frac{h}{2\,\Gamma_\infty^{1/2}}} = \frac{n}{n-1}\,\frac{b_n}{b_\infty}\,\langle d\rangle_\infty\,. \tag{5.16}$$

Figure 11 shows distribution (5.15) plotted with the experimental value $n = 4$ measured in figure 13 together with the experimental size distribution in the spray. From this comparison we see the following.

(i) $\mathfrak{u}_n$ compares much more favourably with measurements than does distribution (5.4), relying on mono-disperse fragmentation of ligaments. The intrinsic ligament dynamics with initial corrugation has a decisive impact on the fragmentation process, and by itself accounts essentially for the overall drop size distribution in the spray.

(ii) $\mathfrak{u}_n$ plotted with the experimental value $n = 4$ does not provide the best description of the measurements, since a slightly smaller order of the gamma distribution $n = 3$ is more accurate. In addition to the dispersions in the ligaments' initial sizes, $\mathfrak{s}(d_l)$, and within each ligament, $\mathfrak{t}_n(d/d_l)$, a third and weaker source of dispersion contributes to the width and shape of the spray distribution: this is the interaction between the ligaments via their connecting node during the breakup period, which is not accounted for here. Nodes do play a role, though not due to geometric effects alone, as discussed in § 5.2, and are responsible for the slight shift from 4 to 3 of the apparent gamma order n.

Another interesting confirmation of the primary role of ligament corrugations comes from the experiments by Reiter (1992) on the dewetting of thin polymer films from a solid substrate. Figure 14 shows the drop pattern observed at the final stage of the dewetting dynamics where the skeleton of the Voronoï cell structure is clearly apparent. The mechanism leading to the formation of isolated droplets is almost the same as ours.

(i) When the polymer is annealed above the glass transition temperature, holes nucleate almost synchronously at a number of heterogeneous location sites.

(ii) The triple lines recede, since the polymer does not wet the substrate, and as a consequence the holes open isotropically by collecting the film liquid into a partially toroidal rim bordering them.

(iii) The rims of neighbouring holes collide and coalesce to form a transient web of ligaments, which subsequently fragment by capillary instability, to give the drop pattern in figure 14.

The only difference from our experiments, which is actually essential as far as the drop dispersion is concerned, is the absence of inertial effects in the receding dynamics of the liquid film. Because the film is so thin and moves on a solid substrate, its motion is completely dominated by viscous effects. The free energy is dissipated all along the rim paths, and when they merge, does not induce additional corrugation to the ligaments, which are thus smooth. We analysed figure 1(*a*) from

https://doi.org/10.1017/jfm.2012.481 Published online by Cambridge University Press

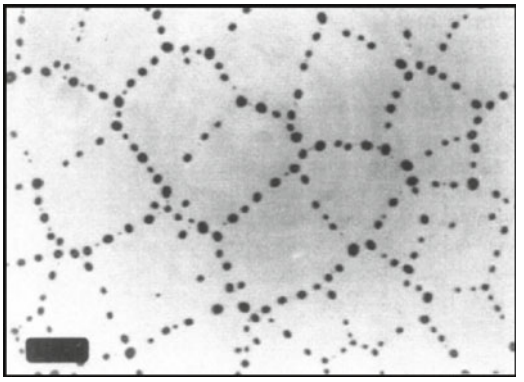


FIGURE 14. (Adapted from figure 1(*a*) in Reiter 1992.) The final stage of the dewetting of a 45 nm thin polystyrene film on a silicon wafer (the black bar is 100 μm long). The Voronoï web, similar to the one observed in the present study, is obvious. The slow dewetting dynamics of this thin viscous film leads to a much narrower droplet size distribution than the inertial film recession of our experiments (see explanations in the text and figure 10 for comparison).

Reiter (1992) (reproduced in figure 14) and measured the drop sizes through the area of their wetting surface (thus assuming a uniform contact angle). The number of drops in the image is too small to obtain a reliable p.d.f., but the relative standard deviation $\sqrt{\langle d^2\rangle}/\langle d\rangle - 1 \simeq 0.31$ we compute from the 220 visible drops is much smaller than 0.68, the one associated with our experimental distribution shown in figure 11. Inertial effects accompanying the merging of the receding rims are definitely responsible for the enhanced dispersion of drop sizes in the global spray.

6. Conclusions and extension

A planar Savart liquid sheet seeded with small air bubbles, on which the fragmentation process can be directly observed step by step and quantified precisely, was studied as a two-dimensional model for 'effervescent' atomization. It was found that the overall sequence of events shaping the connected liquid sheet into a population of disjointed drops proceeds sequentially as: (i) the nucleation of holes; (ii) the formation of a Voronoï web of liquid ligaments at the junction of the grown holes; and (iii) the breakup of the ligaments into drops.

Through this sequence of events the minute fraction of air dispersed in the form of small bubbles into the liquid (less than 0.1 % in volume) was found to have a strong impact on the sheet fragmentation, by reducing both its connected radius R and drop size d, thus illustrating the essence of the 'effervescence' process, depicted here in detail.

Holes nucleate via a Poisson process both in space and time, but the web of liquid ligaments averages out this initial disorder since it results from the addition of the contributions from adjacent holes. The dominant source of disorder explaining the width of the final drop size distribution lies in the intrinsic ligament dynamics which, at breakup, produce a broad collection of drop sizes (according to a gamma distribution), nearly identical to that found in the overall spray. Further comparison with a situation where the intra-ligament dispersion is *de facto* absent emphasized the

https://doi.org/10.1017/jfm.2012.481 Published online by Cambridge University Press

first-order contribution of the size dispersion, within each isolated ligament, promoted by its inertial breakup, to overall spray features.

Although the drops emanating from the web nodes at the junction of three ligaments were found to have a negligible direct contribution to the spray dispersion, the connecting nodes do play a role as they allow drainage from the small ligaments into the largest ones, thus broadening the spectrum of sizes.

The details of the holes' nucleation process were not of direct concern for this study, and nucleation rates in § 3 have been measured but not explained. However, even in the present case of perfectly non-wetting nuclei, namely the bubbles, determining the location of hole formation certainly does not amount to a simple geometric criterion equalizing the bubble diameter with the sheet thickness. This single problem certainly warrants full, careful, fundamental study for heterogeneous nucleation, where the drainage and synchronous puncture of the two liquid lamellas separating the bubble cavity from the atmosphere will have to be elucidated. The configuration of the planar Savart sheet is probably appropriate for that purpose.

Finally, as a bound of the present study, and also an extension toward another possible source of very small drops from this process, we continue the discussion of the role of inertia in rim coalescence at the end of § 5.3. When rims of adjacent holes collide to form a ligament they have relative velocity $2V$. The Weber number associated with the collision of two rims from holes separated by l is then $We \sim \rho V^2 d_l/\sigma \sim \sqrt{l/h}$ and increases with l. If the collision is too intense, namely if We is too large, the rims no longer merge but instead splash, forming a secondary sheet whose orientation is transverse to the original one. As figure 15 illustrates, this secondary sheet is itself bordered by a rim, which subsequently destabilizes and fragments into a collection of droplets much smaller than the source rims' diameters. As a consequence, when the hole density is decreased, everything else being kept constant, the typical diameter d_l of the ligaments at first increases, since they collect more liquid, but paradoxically, above a certain threshold, one expects the diameter d of the resulting drops to actually decrease, since secondary fragmentation will occur.

This new phenomenon naturally sets the domain of validity for the present study, where it was ignored. Indeed, the formation of a web of ligaments resulting from the coalescence of the hole rims *de facto* excludes the formation and fragmentation of these transverse secondary sheets. The present scenario is therefore valid provided that the density in holes β satisfies

$$\frac{16}{\pi^2}\left(\frac{4}{We_c}\right)^4 \lesssim \beta h^2 \lesssim 1, \tag{6.1}$$

where the upper bound expresses that the holes cannot have a diameter smaller than the sheet thickness h (otherwise they would heal instead of expand), whereas the lower bound involves a critical Weber number

$$We_c = \frac{\rho\,(2V)^2\, d_r}{\sigma}, \tag{6.2}$$

based on the rim diameter $d_r = d_l/\sqrt{2}$ and on their relative velocity $2V$, above which a transverse sheet forms and disintegrates. The lower bound in (6.1) involves the fourth power of We_c; it is thus important to consider its precise value.

For the case examined here, direct visualization barely reveals the presence of transverse sheets. The typical Weber number of the collisions is $We = 8\pi^{-1/2}\,(\beta h^2)^{-1/4} \simeq 60$ (defined as in (6.2), where d_l is computed from the mean normal

https://doi.org/10.1017/jfm.2012.481 Published online by Cambridge University Press

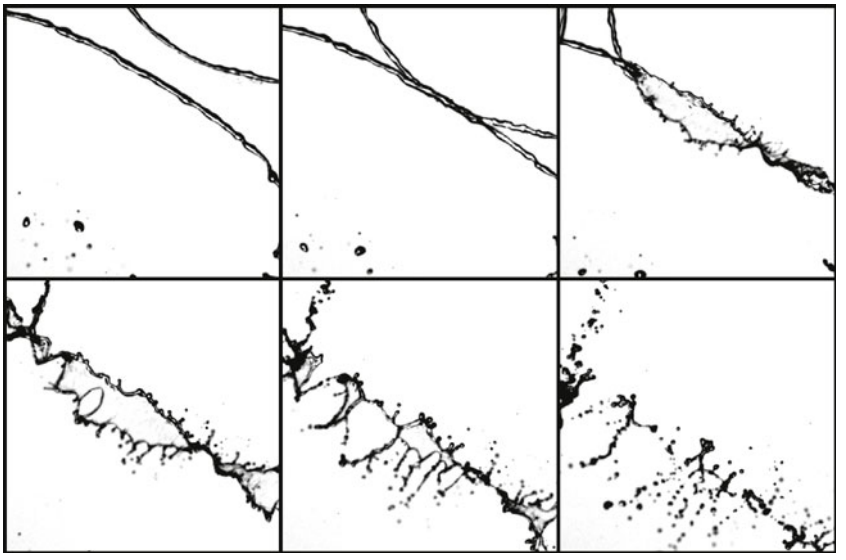


FIGURE 15. Illustration of the impact between two hole bordering rims when hole nucleation is sparse. The rims cover a large distance l prior to collision, resulting in a Weber number of $\sim$280 according to the definition in (6.2). A secondary sheet essentially transverse to the primary one is formed which destabilizes into a series of ligaments (similar to a Worthington crown for drop impact: Worthington & Cole 1897), which in turn resolve into a collection of drops with typical diameter much smaller than those of the rims from which they originate. The images are separated by 1 ms and their width is 36 mm.

distance $\langle l \rangle = \beta^{-1/2}/2$ from (4.2) and $\beta = \Gamma_\infty$ determined in (3.17)). This value is by definition smaller than but certainly close to the critical value We_c, and offers a majoring estimate for the lower bound of the domain of validity defined in (6.1). One can qualitatively relate this critical Weber number to other observations pertaining to the world of drop impacts (note, however, the important difference between the two-dimensional configuration of head-on colliding drops, and the one-dimensional collision of cylinders): Ashgriz & Poo (1990) and later Qian & Law (1997) have measured the threshold Weber number separating the coalescence regime from the post-impact separation of colliding drops for various liquids and ambient pressures. For a head-on collision, they observe that the critical Weber number is approximately 20. The critical Weber number for secondary fragmentation is likely to be above that in the present case, and indeed Villermaux & Bossa (2011) have measured both the maximal radial extent of a drop deforming under impact on a solid target, and the fragments. These could be detected for $We \approx 100$ or slightly below, somewhat closer to our estimate here.

It is clear that this point deserves further investigation; it also offers a natural perspective to the present work. This distinct fragmentation mechanism, at play for small concentrations of nucleation sites, will define a new operating regime for the 'effervescent' atomization process, lying outside from the parameter domain studied here, with expected very small drops resulting from secondary fragmentation, at the cost of a possibly broader size dispersion, because of a larger intermittency in hole nucleation.

https://doi.org/10.1017/jfm.2012.481 Published online by Cambridge University Press

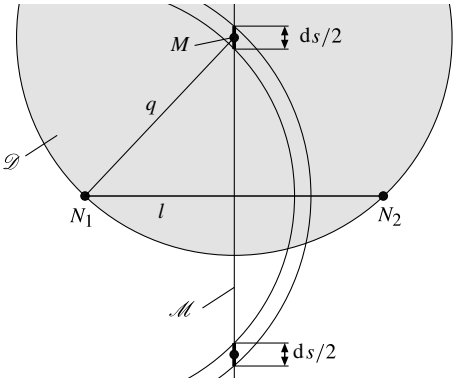


FIGURE 16. N_1 and N_2 are two nucleation sites. The small edge segment with length $\mathrm{d}s/2$ in M on the bisecting line $\mathscr{M}$ of N_1N_2 is part of the Voronoï diagram $\mathscr{V}$ if and only if the grey disk $\mathscr{D}$ centred in M and tangent to N_1 (and thus to N_2) contains no other nucleation site.

Acknowledgements

This work was partially supported by the Office National d'Etudes et Recherches Aérospatiales (ONERA) under contract F/20215/DAT-PPUJ, and by the Agence Nationale de la Recherche (ANR) via grant ANR-05-BLAN-0222-01.

Appendix A. Voronoï statistics

We establish here some results on the statistics of the ligament web resulting from the liquid sheet disintegration in the simplified case where the nucleation over an advected portion of the sheet is concentrated on a short time interval compared with the holes' characteristic growth time, of order $\Gamma_\infty^{-1/2}/V \equiv \beta^{-1/2}/V$. This result is directly applied in §§ 4 and 5 in order to determine the population of drop sizes generated by the 'effervescent' atomization process.

We consider the limit in which the set $\mathscr{N}$ of the nucleation sites appears at $t = 0$ on a sheet assimilated to an infinite and homogeneous two-dimensional space. The nucleation phenomenon is considered to be Poissonian with respect to space, which means that the probability of a hole appearing over a sheet portion with infinitesimal area $\mathrm{d}\Sigma$ depends only on $\mathrm{d}\Sigma$; we denote it by $\beta\,\mathrm{d}\Sigma$. The holes all extend at the same velocity V from the same initial zero size and the same nucleation time, and therefore join at mid-distance between adjacent nucleation sites. The ligament web is then the set $\mathscr{V}$ of the edges of the Voronoï polygons, or 'cells', defined by the points in $\mathscr{N}$ (see figure 10). An arbitrary point M in the plane belongs to the set $\mathscr{V}$ if and only if:

(i) it is at equal distance from two points $\{N_1, N_2\}$ of $\mathscr{N}$;

(ii) and no other point in $\mathscr{N}$ is closer to M than N_1 and N_2, i.e. no other point is included in the disk $\mathscr{D}(M, r)$ of centre M and radius $r = \|\boldsymbol{MN_1}\| = \|\boldsymbol{MN_2}\|$ (see figure 16).

A.1. *Distribution of the ligaments' normal distances l to the nucleation sites*

We determine the expected value (per unit of l) of the perimeter P of an arbitrary cell of the Voronoï diagram which is at a given normal distance l; that is to say the mean length $p(l)$ of the perimeter of a cell that is at a normal distance between l and $l + \mathrm{d}l$ from its nucleation site.

https://doi.org/10.1017/jfm.2012.481 Published online by Cambridge University Press

Let us choose an arbitrary point in the set $\mathscr{N}$ as our origin and call it N_1. The probability that another point of $\mathscr{N}$ exists at a distance between $2\,l$ and $2\,(l+\mathrm{d}l)$ from N_1 (and that therefore an edge will potentially be found between l and $l+\mathrm{d}l$) is

$$p'(l)\,\mathrm{d}l = 8\pi\beta l\,\mathrm{d}l, \tag{A 1}$$

which expresses the likelihood of condition (i) listed above. We assume that this point exists and call it N_2. The probability that a point M lying on the potential edge (the bisecting line $\mathscr{M}$ of N_1N_2 in figure 16) is actually included in $\mathscr{V}$ depends only on its distance q from N_1, and is given by

$$P''(q) = \mathrm{e}^{-\pi\beta q^2}, \tag{A 2}$$

which is the probability that the disk $\mathscr{D}(M,q)$ is empty, thus expressing the likelihood of condition (ii) above. For a given normal distance l of the edge to the centre N_1, the length $\mathrm{d}s$ of the edge which is at a true distance between q and $q+\mathrm{d}q$ from N_1 is simply (see figure 16)

$$\mathrm{d}s = \frac{2}{\sqrt{1-\left(\dfrac{l}{q}\right)^2}}\,\mathrm{d}q. \tag{A 3}$$

Therefore the expected value that an arbitrary portion of the Voronoï diagram $\mathscr{V}$ having an infinitesimal edge length $\mathrm{d}s$ is at a normal distance l from the centre N_1 of its cell is given by integration over all true distances q larger than l, i.e.

$$p(l) = p'(l)\int P''(q)\,\mathrm{d}s = 16\pi\beta l\int_l^\infty \frac{\mathrm{e}^{-\pi\beta q^2}}{\sqrt{1-\left(\dfrac{l}{q}\right)^2}}\,\mathrm{d}q$$

$$= 8\pi\sqrt{\beta}\,l\,\mathrm{e}^{-\pi\beta l^2}. \tag{A 4}$$

In other words $p(l)$ is the mean length of the perimeter of a cell that is at a normal distance l from the cell centre. The average perimeter $\langle P\rangle$ is then given by

$$\langle P\rangle = \int_0^\infty p(l)\,\mathrm{d}l = 4\beta^{-1/2} \tag{A 5}$$

which is consistent with the result of Meijering (1953). Note that (A 4) also yields the mean length of a side $\langle P\rangle/\langle\nu\rangle = (2/3)\beta^{-1/2}$ since the mean number of sides $\langle\nu\rangle$ is 6 for an infinite number of cells in two dimensions, as is known from the Descartes–Euler theorem relating the total number of cells, edges and nodes of a tessellation of the plane.

The sought p.d.f. of the distances l of the ligament portions to the centre of their adjacent cells is then the normalized expected value $p(l)$, i.e.

$$\mathfrak{r}(l) = \frac{p(l)}{\langle P\rangle} = 2\pi\beta\,l\,\mathrm{e}^{-\pi\beta l^2} \tag{A 6}$$

whose mean value is

$$\langle l\rangle = \tfrac{1}{2}\beta^{-1/2}. \tag{A 7}$$

Note that the distribution $\mathfrak{r}(l)$ of normal distances l is not to be confused with the distribution of the true distances or 'radii' q derived by Meijering (1953),

https://doi.org/10.1017/jfm.2012.481 Published online by Cambridge University Press

given by $16\beta\pi q^2 \exp(-\pi\beta q^2)$ (it corresponds to the case $j = 2$ in (A 10)), yielding $\langle q\rangle = (2/\pi)\beta^{-1/2}$.

To our knowledge this result is new. It is directly useful here since it generates the ligament size distribution, but more generally it is potentially useful in every system where a substance concentrates at the periphery of cells dividing a medium. In particular, consider the diverse impurities which preferentially accumulate at the grain boundaries in solidification domains.

A.2. *Distribution of the node distances q to the nucleation sites*

The distribution of the node distances q to the nucleation sites is easier to obtain. More generally, it is actually straightforward to derive the distribution of the distances q from the nucleation sites to the points equidistant from exactly j nucleation sites.

Indeed, the infinitesimal probability that an arbitrary point in the plane has exactly j nucleation sites at a distance between q and $q + \mathrm{d}q$ (the fraction on the right-hand side in the equation below) and no other nucleation site closer (the exponential term), is given by

$$\mathrm{d}^j\Sigma(q) = \frac{(2\pi\beta q\,\mathrm{d}q)^j}{j!}\,\mathrm{e}^{-\pi\beta q^2}, \tag{A 8}$$

which has to be normalized by the infinitesimal probability that an arbitrary point has exactly j equidistant points (to precision $\mathrm{d}q$)

$$\mathrm{d}^{j-1}\Sigma = \int_0^\infty \mathrm{d}^j\Sigma(q)\,\mathrm{d}q, \tag{A 9}$$

to provide the distribution $\mathfrak{v}(q) = \mathrm{d}^j\Sigma(q)/\mathrm{d}^{j-1}\Sigma$, i.e.

$$\left.\begin{aligned} \mathfrak{v}(q) &= \frac{2\,(\pi\beta)^{(j+1)/2}}{\Gamma\left(\dfrac{j+1}{2}\right)}\,q^j\,\mathrm{e}^{-\pi\beta q^2}, \\ \langle q\rangle &= \frac{\Gamma\left(\dfrac{j}{2}+1\right)}{\sqrt{\pi\beta}\,\Gamma\left(\dfrac{j+1}{2}\right)}. \end{aligned}\right\} \tag{A 10}$$

The sought distribution for the distances q to the nodes is then obtained by imposing $j = 3$, giving

$$\left.\begin{aligned} \mathfrak{v}(q) &= 2\,(\pi\beta)^2\;q^3\mathrm{e}^{-\pi\beta q^2}, \\ \langle q\rangle &= \tfrac{3}{4}\beta^{-1/2}, \end{aligned}\right\} \tag{A 11}$$

since in two dimensions each node is equidistant from exactly three nucleation sites.

REFERENCES

ASHGRIZ, N. & POO, J. Y. 1990 Coalescence and separation in binary collisions of liquid drops. *J. Fluid Mech.* **221**, 183–204.

AVRAMI, M. 1939 Kinetics of phase change. Part 1. General theory. *J. Chem. Phys.* **7**, 1103–1112.

AVRAMI, M. 1940 Kinetics of phase change. Part 2. Transformation-time relations for random distribution of nuclei. *J. Chem. Phys.* **8**, 212–224.

https://doi.org/10.1017/jfm.2012.481 Published online by Cambridge University Press

AVRAMI, M. 1941 Kinetics of phase change. Part 3. Granulation, phase change, and microstructure. *J. Chem. Phys.* **9**, 177–184.

BESKOW, K., THORÉN, M. & LUNDSTRÖM, P.-A. 2009 World's first high-capacity Granshot® iron granulation in operation at SSAB Oxelösund. *AISTech 2009 Proceedings* **1**, 211–218.

BOHR, N. 1909 Determination of the surface-tension of water by the method of jet vibration. *Phil. Trans. R. Soc. Lond.* A **209**, 281–317.

BREMOND, N., CLANET, C. & VILLERMAUX, E. 2007 Atomization of undulating liquid sheets. *J. Fluid Mech.* **585**, 421–456.

BREMOND, N. & VILLERMAUX, E. 2005 Bursting thin liquid films. *J. Fluid Mech.* **524**, 121–130.

BREMOND, N. & VILLERMAUX, E. 2006 Atomization by jet impact. *J. Fluid Mech.* **549**, 273–306.

CLANET, C. & VILLERMAUX, E. 2002 Life of a smooth liquid sheet. *J. Fluid Mech.* **462**, 307–340.

CLAY, P. 1940 The mechanism of emulsion formation in turbulent flow. Part 1. Experimental part. *Proc. R. Acad. Sci. (Amsterdam)* **43**, 852–865.

COUDER, Y., CHOMAZ, J. & RABAUD, M. 1989 On the hydrodynamics of soap films. *Physica* D **37**, 384–405.

CULICK, F. E. C. 1960 Comments on a ruptured soap film. *J. Appl. Phys.* **31**, 1128.

DAVIES, J. T. & RIDEAL, E. K. 1963 *Interfacial Phenomena*, 2nd edn. Academic.

DOMBROWSKI, N. & FRASER, R. P. 1954 A photographic investigation into the disintegration of liquid sheets. *Phil. Trans. R. Soc. Lond.* A **247**, 101–130.

EINSTEIN, A. 1906 Eine neue Bestimmung der Moleküldimensionen. *Ann. Phys.* **19** (4), 289–306.

HINZE, J. 1949 Fundamentals of the hydrodynamic mechanism of splitting in dispersion processes. *AIChE J.* **1**, 289–295.

HUANG, J. C. P. 1970 The break-up of axisymmetric liquid sheets. *J. Fluid Mech.* **43**, 305–319.

JOHNSON, W. A. & MEHL, R. F. 1939 Reaction kinetics in processes of nucleation and growth. *Trans. AIME* **135**, 416–443.

KOLMOGOROV, A. 1941 The local structure of turbulence in incompressible viscous fluid for very large Reynolds' numbers. *Dokl. Akad. Nauk SSSR* **30**, 301.

KOLMOGOROV, A. 1949 On the breakage of drops in a turbulent flow. *Dokl. Akad. Nauk SSSR* **66**, 825–828.

LEFEBVRE, A. H. 1989 *Atomization and Sprays*. Hemisphere.

LIDE, D. R. (Ed.) 1999 *Handbook of Chemistry and Physics*, 79th edn. CRC.

LORD RAYLEIGH, 1878 On the instability of jets. *Proc. R. Soc. Lond.* A **10**, 4–13.

LORD RAYLEIGH, 1890 On the tension of recently formed liquid surfaces. *Proc. R. Soc. Lond.* A **47**, 281–287.

MARMOTTANT, P. & VILLERMAUX, E. 2004 On spray formation. *J. Fluid Mech.* **498**, 73–111.

MARMOTTANT, P., VILLERMAUX, E. & CLANET, C. 2000 Transient surface tension of an expanding liquid sheet. *J. Colloid Interface Sci.* **230**, 29–40.

MEIJERING, J. L. 1953 Interface area, edge length and number of vertices in crystal aggregates with random nucleation. *Philips Res. Rep.* **8**, 270–290.

NAGATA, S. 1975 *Mixing, Principles and Applications*. Wiley.

QIAN, J. & LAW, C. K. 1997 Regimes of coalescence and separation in droplet collision. *J. Fluid Mech.* **331**, 59–80.

REITER, G. 1992 Dewetting of thin polymer films. *Phys. Rev. Lett.* **68**, 75–78.

ROZHKOV, A., PRUNET-FOCH, B. & VIGNES-ADLER, M. 2004 Dynamics of a liquid lamella resulting from the impact of a water drop on a small target. *Proc. R. Soc. Lond.* A **460**, 2681–2704.

ROZHKOV, A., PRUNET-FOCH, B. & VIGNES-ADLER, M. 2010 Impact of drops of surfactant solutions on small targets. *Proc. R. Soc. Lond.* A **466** (2122), 2897–2916.

SANTALÓ, L. 2004 *Integral Geometry and Geometric Probability*, 2nd edn. Cambridge University Press.

SAVART, F. 1833*a* Mémoire sur le choc d'une veine liquide lancée contre un plan circulaire. *Ann. Chim.* **54**, 56–87.

https://doi.org/10.1017/jfm.2012.481 Published online by Cambridge University Press

SAVART, F. 1833*b* Suite du mémoire sur le choc d'une veine liquide lancée contre un plan circulaire. *Ann. Chim.* **54**, 113–145.

SOVANI, S., SOJKA, P. & LEFEBVRE, A. 2001 Effervescent atomization. *Prog. Energy Combust. Sci.* **27**, 483–521.

TAYLOR, G. I. 1932 The viscosity of a fluid containing small drops of another fluid. *Proc. R. Soc. Lond.* A **138**, 41–48.

TAYLOR, G. I. 1959 The dynamics of thin sheets of fluid. Part 1. Water bells. *Proc. R. Soc. Lond.* A **253**, 289–295.

TAYLOR, G. I. & MICHAEL, D. H. 1973 On making holes in a sheet of fluid. *J. Fluid Mech.* **58** (4), 625–639.

THORODDSEN, S. T., ETOH, T. G. & TAKEHARA, K. 2006 Crown breakup by Marangoni instability. *J. Fluid Mech.* **557**, 63–72.

VILLERMAUX, E. & BOSSA, B. 2011 Drop fragmentation on impact. *J. Fluid Mech.* **668**, 412–435.

VILLERMAUX, E. & CLANET, C. 2002 Life of a flapping liquid sheet. *J. Fluid Mech.* **462**, 342–363.

VILLERMAUX, E., MARMOTTANT, P. & DUPLAT, J. 2004 Ligament-mediated spray formation. *Phys. Rev. Lett.* **92** (7).

WORTHINGTON, A. M. & COLE, R. S. 1897 Impact with a liquid surface, studied by the aid of instantaneous photography. *Phil. Trans. R. Soc. Lond.* A **189**, 149–166.

YULE, A. J. & DUNKLEY, J. J. 1994 *Atomization of Melts*. Clarendon.

https://doi.org/10.1017/jfm.2012.481 Published online by Cambridge University Press